Supporting Information

Anion Extraction-Induced Polymorph Control of Transition Metal Dichalcogenides

Dae-Hyun Nam,[†,§] Ji-Yong Kim,[†,§] Sungwoo Kang,[†,§] Wonhyo Joo,[†] Seung-Yong Lee,[†] Hongmin Seo,[†] Hyoung Gyun Kim,[†] In-Kyoung Ahn,[†] Gi-Baek Lee,[†] Minjeong Choi,[†] Eunsoo Cho,[†] Miyoung Kim,[†,‡] Ki Tae Nam,[†,‡] Seungwu Han,[†,‡] and Young-Chang Joo[,†,‡]*

[†]Department of Materials Science and Engineering, Seoul National University, 1 Gwanak-ro, Gwanak-gu, Seoul 08826, Republic of Korea

[‡]Research Institute of Advanced Materials (RIAM), Seoul National University, 1 Gwanak-ro, Gwanak-gu, Seoul 08826, Republic of Korea

[§]These authors contributed equally to this work.

*Corresponding author, E-mail: ycjoo@snu.ac.kr

1. Materials and methods

DFT calculation. The density functional theory (DFT) calculations were performed using the Vienna Ab initio Simulation Package (VASP). The projector augmented wave (PAW) method was implemented to consider electron-ion interactions. The generalized gradient approximation was used for the exchange-correlation functional. The energy cutoff for the plane-wave basis was set to 400 eV. The simulations are performed in a 4×4 and 2×4 supercell for 2H-molybdenum disulfide (MoS_2) and 1T′-MoS_2, respectively. We assume that vacancies are generated both sides of the MoS_2. The Brillouin zone was sampled by 9×9×1 and 3×3×1 k point meshes for unit cells and 4×4 supercells, respectively. The atomic structures of each simulation cell were relaxed until all forces on the atoms were reduced to within 0.03 eV/Å.

Thermodynamic calculation. The ternary phase diagrams and product distributions were calculated using a thermochemical database program (Factsage™ software). We used the FACT pure substances database (FactPS) and the FACT light metal database (FTlite). The MoS_2-carbon monoxide (CO)-carbon dioxide (CO_2) ternary phase diagram with tie lines was calculated at the pressure and temperature conditions of 760 Torr and 800 °C. A contour map of the product distribution (Mo sulfide, Mo oxide, Mo carbide, and carbon) was constructed according to the combination of starting materials (MoS_2 (s), CO (g), and CO_2 (g)). The processing conditions of the CO:CO_2 relative ratio and the MoS_2 mass necessary to induce Mo sulfidation while preventing other reactions were determined by thermodynamic calculation. The gas and solid product evolution according to the CO ratio was plotted by calculating the Gibbs free energy of each compound. The thermodynamic calculations were carried out with the assumption of an infinite calcination time.

Material fabrication and calcination. Conventional MoS_2 powder (Mw=160.07 g/mol) was purchased from Sigma-Aldrich. For the fabrication of the MoS_2/CNFs by electrospinning, ammonium tetrathiomolybdate (ATTM, $(NH_4)_2MoS_4$, Mw=260.28 g/mol, Sigma-Aldrich) and polyacrylonitrile (PAN, C_3H_3N, Mw=150,000 g/mol, Sigma-Aldrich) solutions were prepared by dissolving 1.4 g ATTM in 5 g N,N-dimethylformamide (DMF, Sigma-Aldrich) and dissolving 0.7855 g PAN in 5 g DMF with stirring at 120 °C for 2 h. The ATTM solution and PAN solution were then mixed and stirred for 10 h. After loading the mixed ATTM + PAN solution into a syringe, electrospinning was carried out at a controlled rate of 0.3 mL/h using a syringe pump (KDS 100, KD Scientific) and an applied potential of 15 kV generated by a voltage source. The MoS_2 powders and electrospun MoS_2/CNFs were calcined at 800 °C under CO/CO_2 gas flow ambient conditions. The CO to CO_2 gas ratio was controlled by mass flow meters (MFC), and the gases were flowed simultaneously to the chamber.

Material characterization. The morphology and atomic arrangement of the MoS_2 layers were analyzed by transmission electron microscopy (TEM, Tecnai F20, FEI, JEM-2100F, JEOL) and Cs-corrected transmission electron microscopy (cs-TEM, JEM-ARF200F, JEOL). For the TEM sample preparation, the MoS_2 powders and MoS_2/CNFs were sonicated in methanol, and the dispersed solution was dropped on a TEM grid and dried. The ratio of 1T-MoS_2 to 2H-MoS_2 was investigated by X-ray photoelectron spectroscopy (XPS, PHI 5000 VersaProbe, Ulvac-PHI). The XPS spectra were calibrated by the C 1s peak at 284.8. The formation of 1T-MoS_2 was confirmed by Raman analysis (LabRAM HV Evolution, HORIBA). The MoS_2 phase was analyzed by X-ray diffraction (XRD, New D8 Advance, Bruker). The oxidation states and local atomic structure of MoS_2 were investigated by X-ray absorption spectroscopy (XAS) at the Mo K-edge. The XAS

analysis was performed at the 8C – Nano XAFS beamline at the Pohang light source (PLS-II). X-ray absorption near edge structure (XANES) and EXAFS data processing was performed using the ATHENA program. Structural information, including the Mo-S coordination number and atomic distance, was calculated by fitting EXAFS spectra with the ARTEMIS program.

Electrochemical measurement. The effect of the 1T-MoS_2 phase on the hydrogen evolution reaction (HER) activity of the MoS_2/CNFs was investigated in a three-electrode electrochemical H-cell with a 0.5 M H_2SO_4 electrolyte. A saturated calomel electrode (SCE) and Pt wire were used as the reference electrode and counter electrode, respectively. The SCE was converted to a reversible hydrogen electrode (RHE) based on the equation E(RHE) = E(SCE) + 0.242 + 0.059*pH. The iR correction proceeded using the resistance of 5 Ω, which is the solution resistance of 0.5 M H_2SO_4 at room temperature[1]. A total of 8 mg MoS_2/CNFs was dispersed in a solution of 200 μL ethanol (C_2H_5OH) + 800 μL deionized (DI) water + 80 μL Nafion (Nafion perfluorinated resin solution, 5 wt.% in a mixture of lower aliphatic alcohols and water, Sigma-Aldrich), and the solution was sonicated for 30 min. The working electrode was prepared by dropping 5 μL solution ink on a glassy carbon electrode (GCE, 3 mm diameter, CHI 104, CH Instrument) and drying it. LSV with a range from 0 to -0.6 V (vs. RHE) was performed with a scan rate of 2 mV/s.

2. Theoretical simulation of 1T-MoS_2 conversion according to the COS formation

To verify the S extraction from MoS_2 by CO/CO_2 calcination, we simulated the gas and solid products that are generated as the CO ratio increases (modeling condition: 10^4 mol CO/CO_2 mixed gas per 1 mol MoS_2). The formable gas products were predicted to be carbon disulfide (CS_2), sulfur dioxide (SO_2), and carbonyl sulfide (COS) (Figure S4a). After the early stage of diminishing S_2

and SO_2, COS was generated with the increasing CO amount (Figure S4b). The amount of MoS_2 decreased in accordance with the increasing COS amount (Figure S4c). Considering Eq. (1), which describes the formation of $MoS_{2-\delta}$ by the MoS_2-CO reaction, a possible CO (g) reaction with the S in MoS_2 to generate V_S and COS (g) was predicted.

3. Raman analysis

To verify the 1T phase conversion, we carried out the Raman analysis of the MoS_2 powder with CO ratio of 40% (Figure S9) and MoS_2/CNFs after 5 h calcination with CO ratios of 30, 40, and 60% (Figure S13). They showed clear Raman peaks of J_1, J_2, and J_3, which indicate the existence of the 1T phase.[2] Compared to the 30 and 40% CO ratios, the relative Raman peak intensity of MoS_2 at the 60% CO, 5 h condition was low. This result is in agreement with the 1T-MoS_2 formation tendency in the XPS analysis.

4. Gas detection experiment

100 mL of outlet gas from the tube furnace was extracted at 800 °C using gas collector, and we injected the collected gas to the detectors. The initial color of COS, SO_2, and CS_2 gas detectors was blue and the color changed from blue to yellow when the gas was detected. We determined the amount of each gas by the portion of yellow region. Gaseous species were detected during the CO/CO_2 calcination of MoS_2 powders and MoS_2/CNFs. The CO/CO_2 calcination of MoS_2 powders for polymorph conversion (800 °C, 40% CO condition) induced the formation of COS, SO_2, and CS_2 gases (Figure S11). COS gas was detected at the temperature ramping region of 200 and 430 °C. It is expected that S extraction (V_S formation) starts at the ramping region of calcination. When we changed the CO ratio (30, 40, 60% CO) in the calcination of MoS_2/CNFs, the amount

of each COS, SO_2, and CS_2 gas was changed accordingly and this trend was similar with the theoretical calculation (Figure S21). As the CO ratio increased, the amount of COS increased (reaction between CO and S in MoS_2). As the CO ratio increased, the amount of SO_2 decreased. This can be explained by the oxygen partial pressure (pO_2) controlled by the equilibrium between CO and CO_2. Also, the amount of CS_2 increased up to 40% CO and decreased at 60% CO. We expect that it is related with the promoted COS formation at 60% CO condition, which can be competitive with CS_2 formation.

5. XANES analysis of 1T-MoS_2/CNFs to investigate the oxidation state of Mo

The Mo oxidation states were identical in the MoS_2/CNFs calcined under 25, 30, and 40% CO ratios at the 1 h and 5 h condition (Figure S15, S16). However, in 5 h, the Mo ions in the MoS_2/CNFs of the 60% CO condition exhibited a higher oxidation state than the others. It seems that this oxidation state difference may affect the decreased degree of polymorph transition toward the T phase in the 60% CO, 5 h calcination.

6. Effect of calcination temperature on 1T-MoS_2 formation

We compared the deconvolution of the Mo 3d XPS spectra of the MoS_2/CNFs at the 40% CO and 5 h calcination at 600, 800, and 1000 °C (Figure S23). The 1T-MoS_2 ratio increased from 23.1% to 69.4% as the calcination temperature decreased from 1000 to 600 °C. The processing parameter (CO ratio, isothermal time, and temperature)-based systematic controllability of this method enables the property optimization of MoS_2 according to the application.

7. Determination of edge energy and nanoparticle morphology for DFT calculations

The edge energies of 2H- and 1T′-MoS_2 were calculated using a ribbon and a nanoparticle model. First, we determine the edge configuration via the same method as in ref. S3[3] and S4[4] using the ribbon model (Figure S24a). The most stable edge terminations of 2H-MoS_2 and 1T′-MoS_2 were 25% sulfidated (Figure 4d, e). As the ribbon model in Figure S24a and Figure 4d (in the main text) inevitably includes both the Mo-edge and S-edge, we calculate the edge energy of the 2H-MoS_2 nanoparticle, which only includes the 50% terminated Mo-edge (Figure S24b). Table S6 shows the energy of 50% terminated Mo-edge of the nanoparticle with respect to the size of the particle. The edge energy was well converged. Then, the 50% terminated S-edge energy was calculated using the ribbon model from Figure S24a. The edge energies of the 50% terminated Mo-edge and S-edge were calculated to be 0.60 eV/Å and 0.40 eV/Å, respectively. Then, energies of 25% terminated Mo-edge and S-edge were calculated using the ribbon structure in Figure 4d in the main text. Both edges in ribbon model of 1T′-MoS_2 are identical, therefore we calculated edge energies of 1T′-MoS_2 directly by the ribbon model in Figure 4e in the main text.

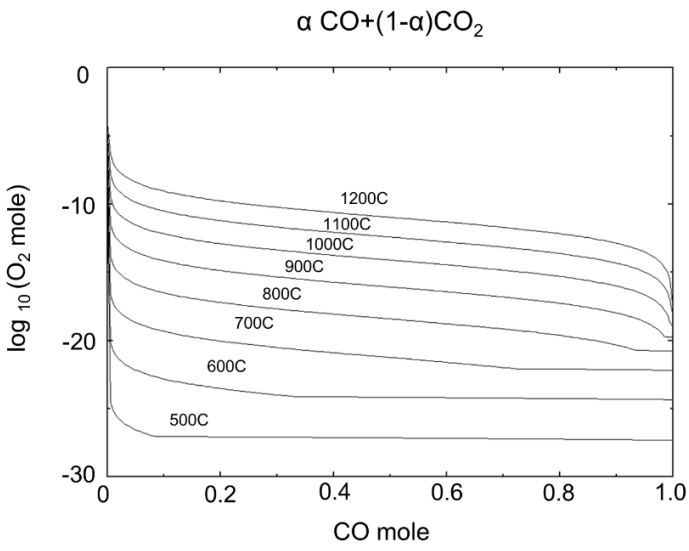

Figure S1. Thermodynamic calculation for controlled pO_2 by the relative ratio between CO and CO_2. pO_2, controlled by interaction between CO and CO_2, was predicted by Factsage^{TM} based thermodynamic calculation according to the CO/CO_2 relative ratio, and calcination temperature. The relative ratio control between CO and CO_2 at a specific temperature enabled to control the pO_2 without vacuum.

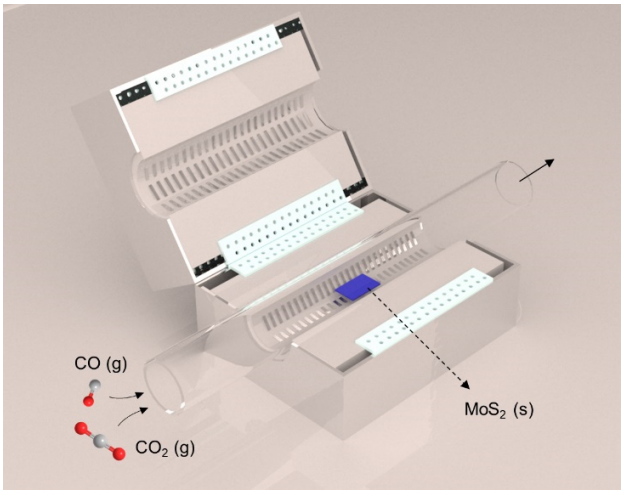

Figure S2. Schematic for displaying the furnace system. The reaction between CO and MoS_2 occurs at the furnace to the formation of 1T-MoS_2. We detected pO_2 by yttria-stabilized-zirconia (YSZ) sensor at the outlet.

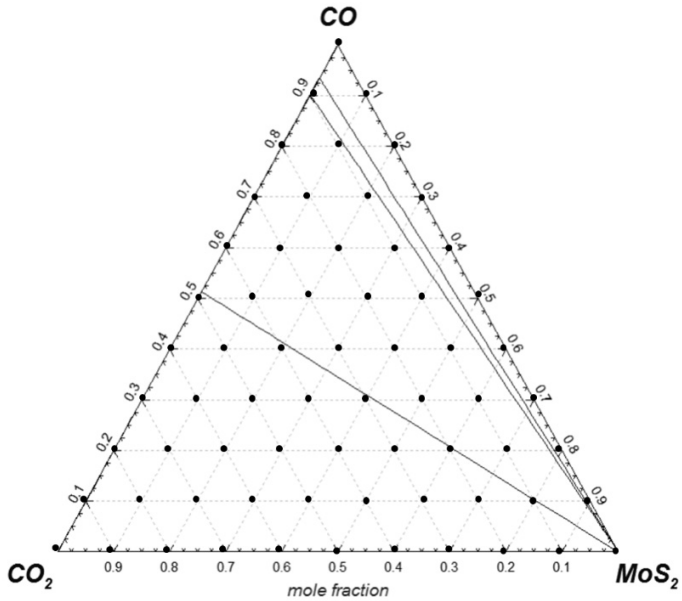

Figure S3. Product calculation after CO/CO_2 calcination of MoS_2. Reaction products were calculated by the compositions of MoS_2-CO-CO_2 marked in ternary phase diagram for designing 1T-MoS_2 formation processing window.

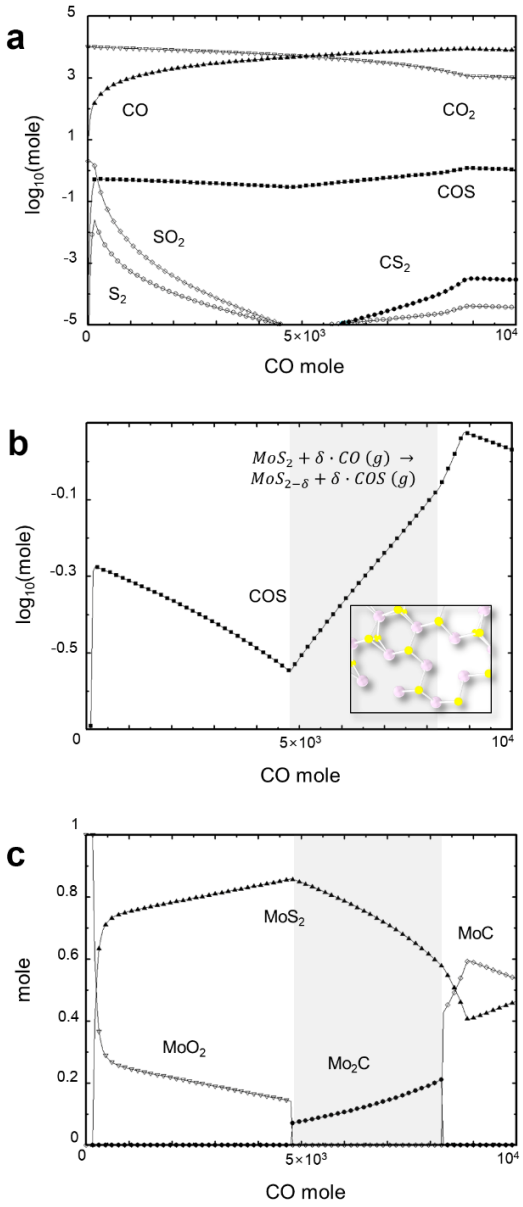

Figure S4. Thermodynamic prediction for processing parameter window. V_S-induced 1T-MoS_2 formation can be predicted by the calculated amount of (a) gaseous products, (b) COS gas, and (c) solid products calculated according to the CO amount.

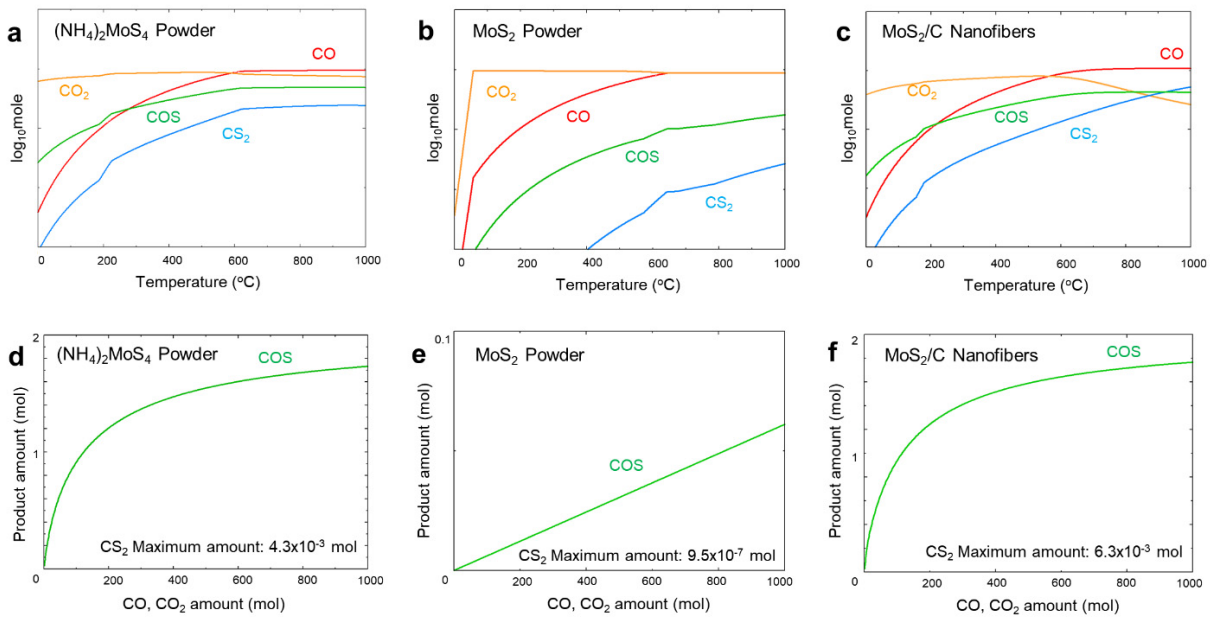

Figure S5. Thermodynamically calculated gaseous products after CO/CO_2 calcination. Factsage™ calculation according to the reaction temperature in various MoS_2 material types: (a) $(NH_4)_2MoS_4$ powder, (b) MoS_2 powder, and (c) MoS_2/CNFs. The degree of COS formation which reveals the reaction between CO and S atom in MoS_2 increases according to the CO/CO_2 gas amounts: (d) $(NH_4)_2MoS_4$ powder, (e) MoS_2 powder, and (f) MoS_2/CNFs. Calcination under CO/CO_2 is expected to change the MoS_2 polymorph regardless of the MoS_2 form factor.

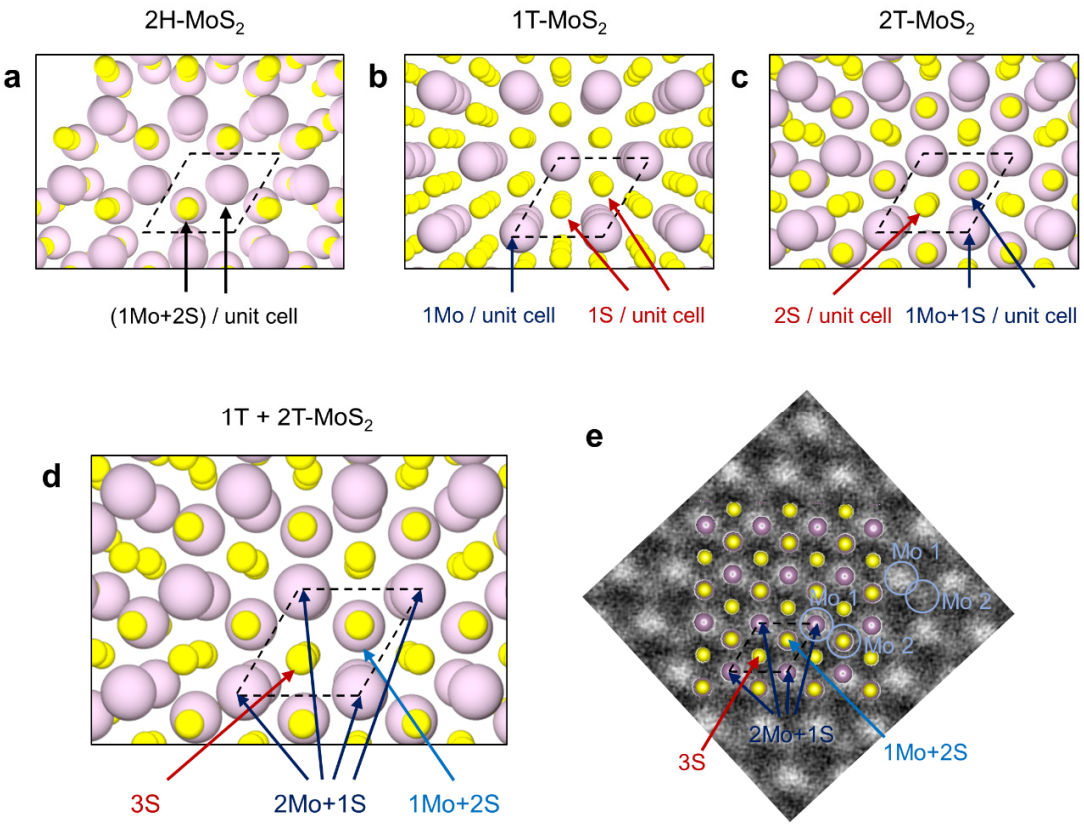

Figure S6. MoS_2 structure investigation according to polymorph. MoS_2 atomic structure model in c-axis direction of (a) 2H-MoS_2, (b) 1T-MoS_2, (c) 2T-MoS_2, and (d) 1T + 2T MoS_2. (e) HAADF-STEM image for displaying the atomic arrangement of MoS_2 layers exfoliated from MoS_2 powder after CO/CO_2 calcination. In 2H-MoS_2, 1 Mo and 2 S atoms exist per unit cell in the column direction. 1 Mo and 1 S atoms exist in 1T-MoS_2, and 1 Mo and 1 S, 2 S atoms exist in 2T-MoS_2. There is a brightness difference in Mo 1 and Mo 2 site. It is because more Mo atoms which is heavier than S exist in Mo 1 site. It can be explained by the coexistence of 1T- and 2T-MoS_2 structures.[5]

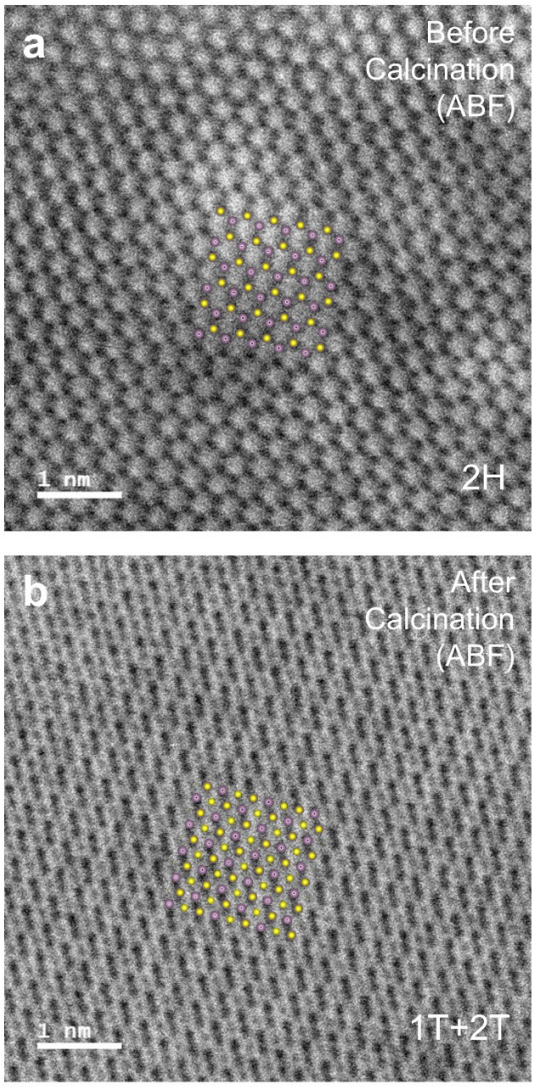

Figure S7. Annular Bright Field (ABF) STEM analysis of MoS_2 layers. ABF-STEM images of MoS_2 exfoliated from MoS_2 powder to compare the atomic arrangement between (a) before and (b) after CO/CO_2 calcination (40% CO) at 800 °C for 5 h. Purple color is for Mo and yellow color is for S.

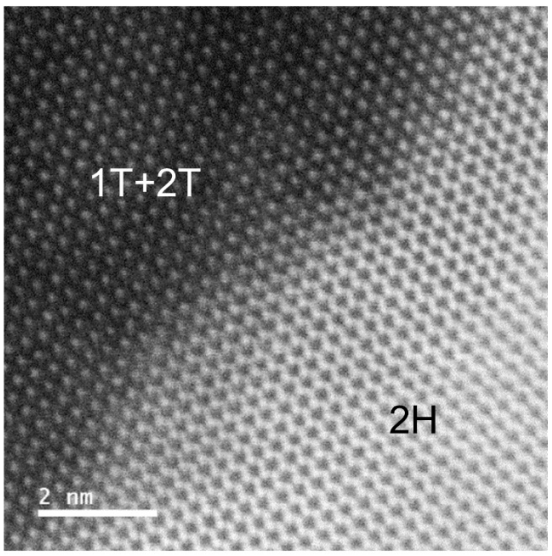

Figure S8. HAADF-STEM image of MoS_2 powders after CO/CO_2 calcination (40% CO, 800 °C, 5 h condition). The interface between 1T+2T-MoS_2 and 2H-MoS_2 after calcination indicates the co-existence of both phases in the flake.

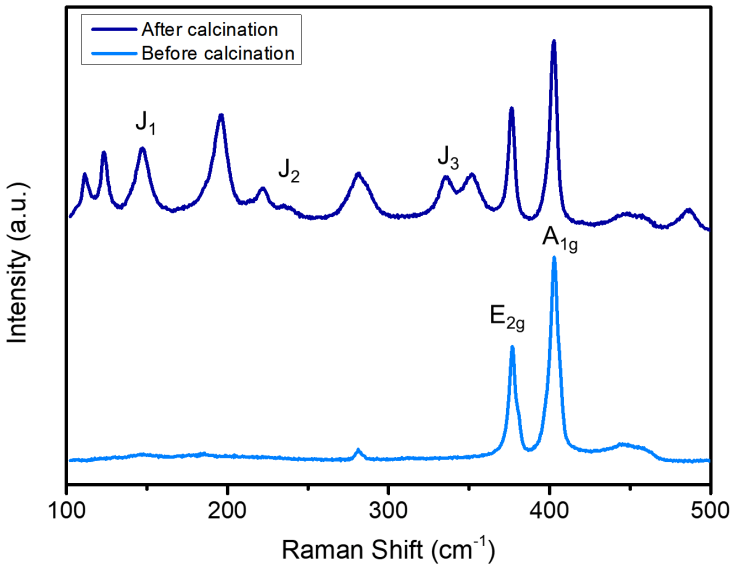

Figure S9. Raman analysis for the verification of 1T-MoS_2 formation in MoS_2 powder after the CO/CO_2 calcination (40% CO) at 800 °C for 5 h.

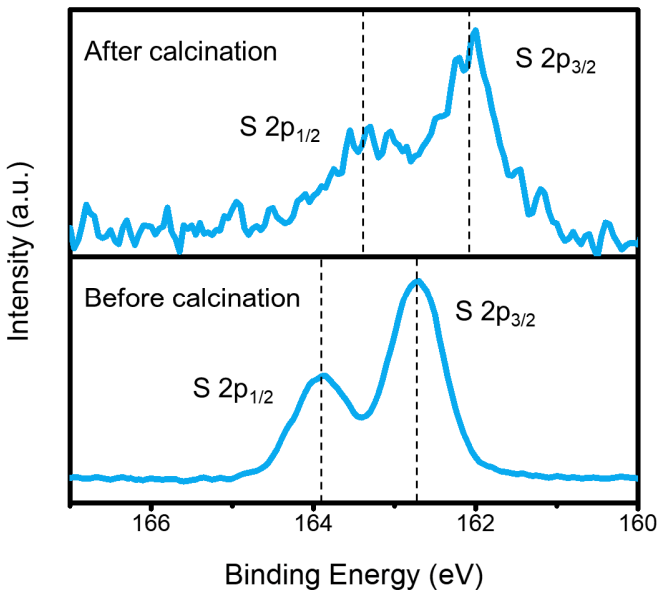

Figure S10. S 2p XPS analysis of MoS_2 powders before and after the CO/CO_2 calcination (40% CO, 800 °C, and 5 h condition).

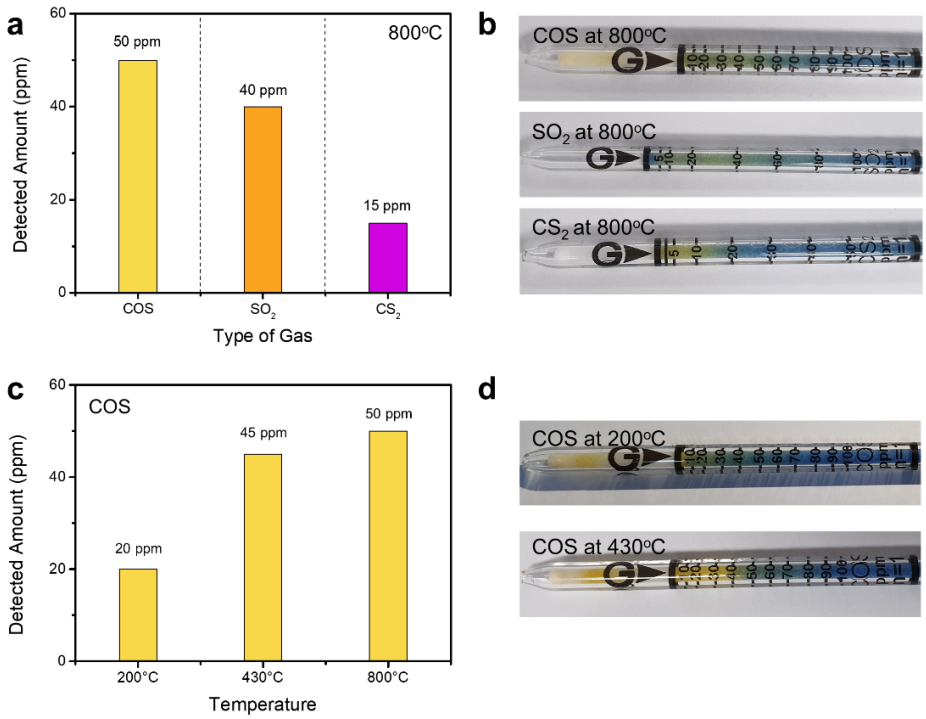

Figure S11. Gas detection during the CO/CO_2 calcination of MoS_2 powders. (a) Detected amount of COS, SO_2, and CS_2 gases during the calcination at the condition of 40% CO and 800 °C. (b) Photographs of the COS, SO_2, and CS_2 gas detectors. (c) Detected amount of COS gas according to the calcination temperature in the ramping region (40% CO). (d) Photographs of the COS gas detectors to measure COS amount according to calcination temperature.

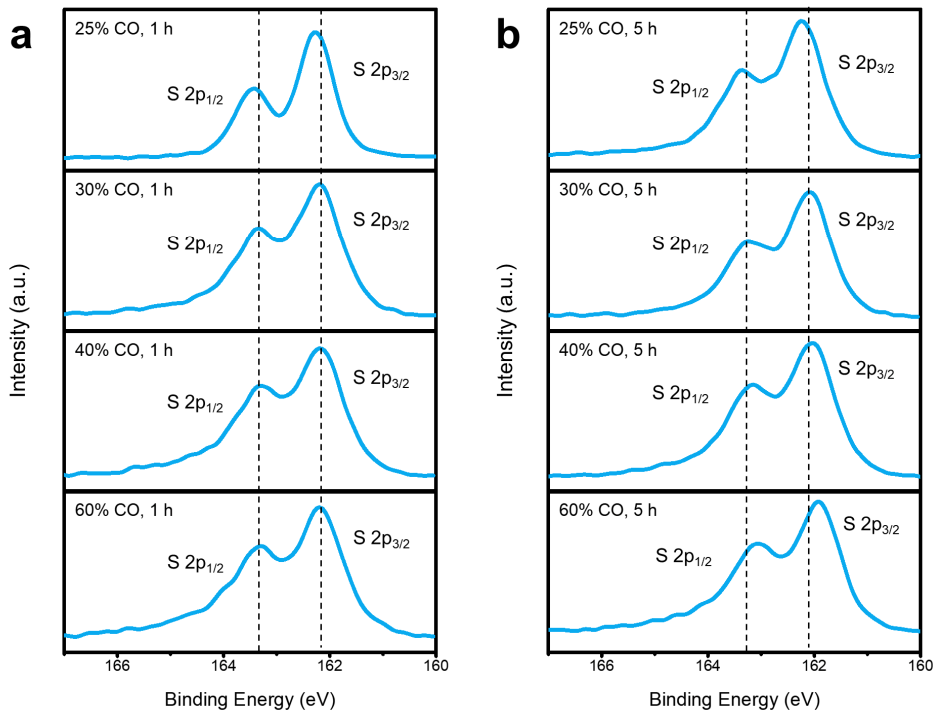

Figure S12. S 2p XPS spectra of MoS_2/CNFs according to the CO ratio at calcination isothermal times of (a) 1 h and (b) 5 h at 800 °C.

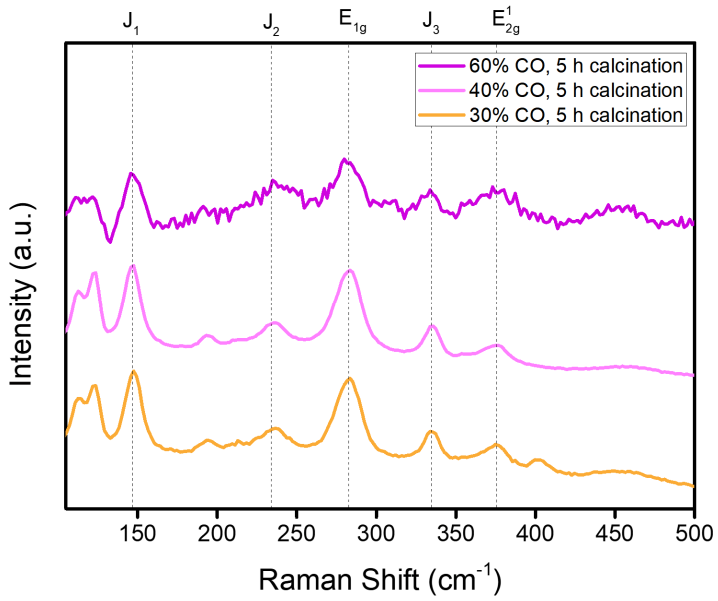

Figure S13. Raman analysis for the verification of 1T-MoS_2 formation in MoS_2/CNFs after the CO/CO_2 calcination (30, 40, and 60% CO) at 800 °C for 5 h.

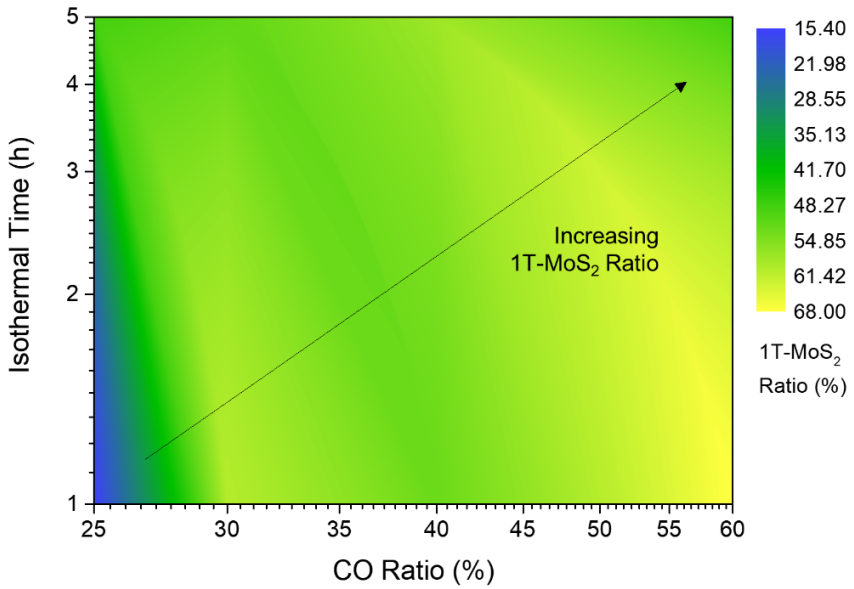

Figure S14. Contour map for investigating the 1T-MoS_2 formation according to processing parameters. 1T-MoS_2 formation map of MoS_2/CNFs is established by the deconvolution of Mo 3d XPS according to the isothermal time and CO ratio of the CO+CO_2 mixture gas in the calcination.

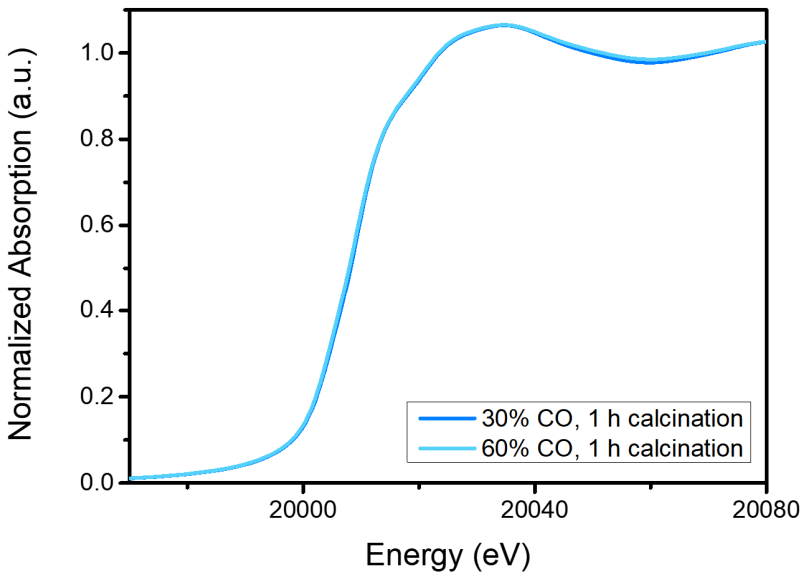

Figure S15. Mo K-edge XANES spectra for investigating the Mo oxidation states of MoS_2 in MoS_2/CNFs according to the CO ratio of 30 and 60% during 1 h calcination.

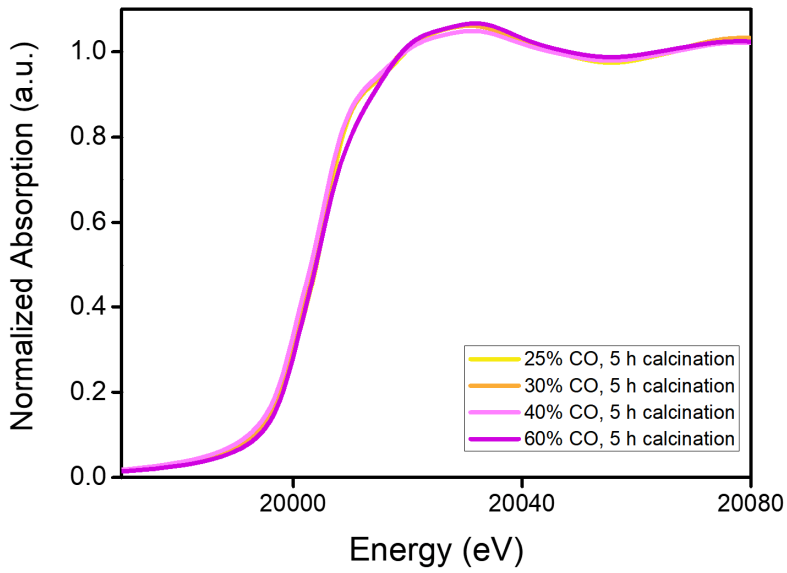

Figure S16. Mo K-edge XANES spectra for investigating the Mo oxidation states of MoS_2 in MoS_2/CNFs according to the CO ratio of 25, 30, 40, and 60% during 5 h calcination.

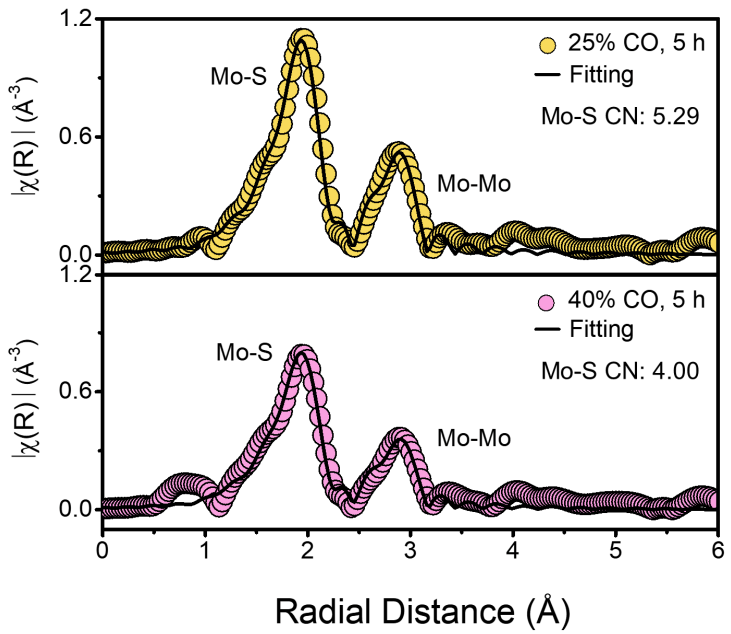

Figure S17. Mo K-edge EXAFS spectra with fitting for investigating the local atomic structures (coordination number, atomic distance) of Mo-S in MoS_2/CNFs according to the CO ratio (25% and 40%) after 5 h calcination.

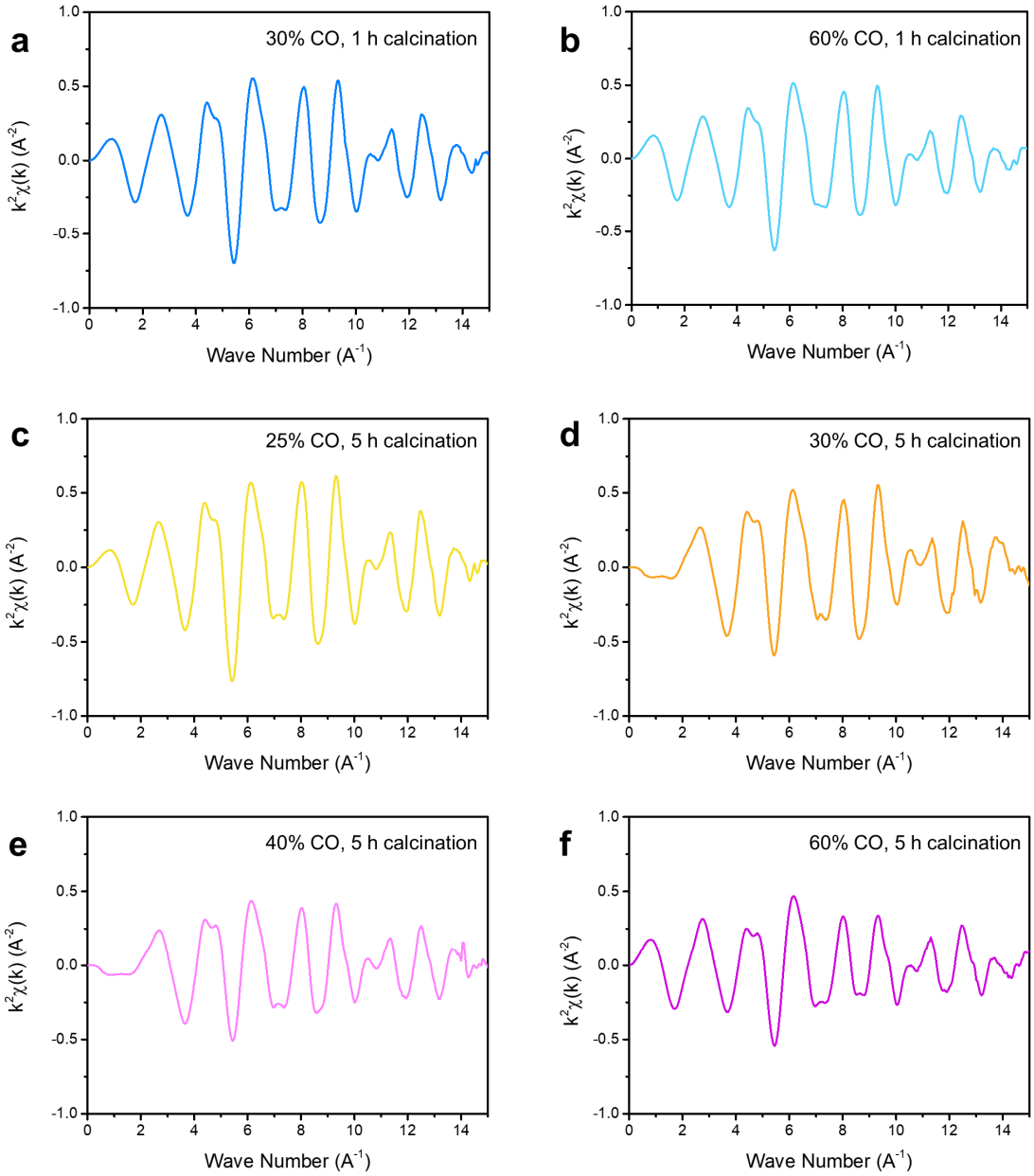

Figure S18. Mo-K edge EXAFS oscillation function $k^2\chi(k)$ of MoS_2 in MoS_2/CNFs. $k^2\chi(k)$ of MoS_2 in MoS_2/CNFs was investigated according to the CO/CO_2 calcination processing parameters. (a) 30% CO, 1 h, (b) 60% CO, 1 h, (c) 25% CO, 5 h, (d) 30% CO, 5 h, (e) 40% CO, 5 h, and (f) 60% CO, 5 h calcination.

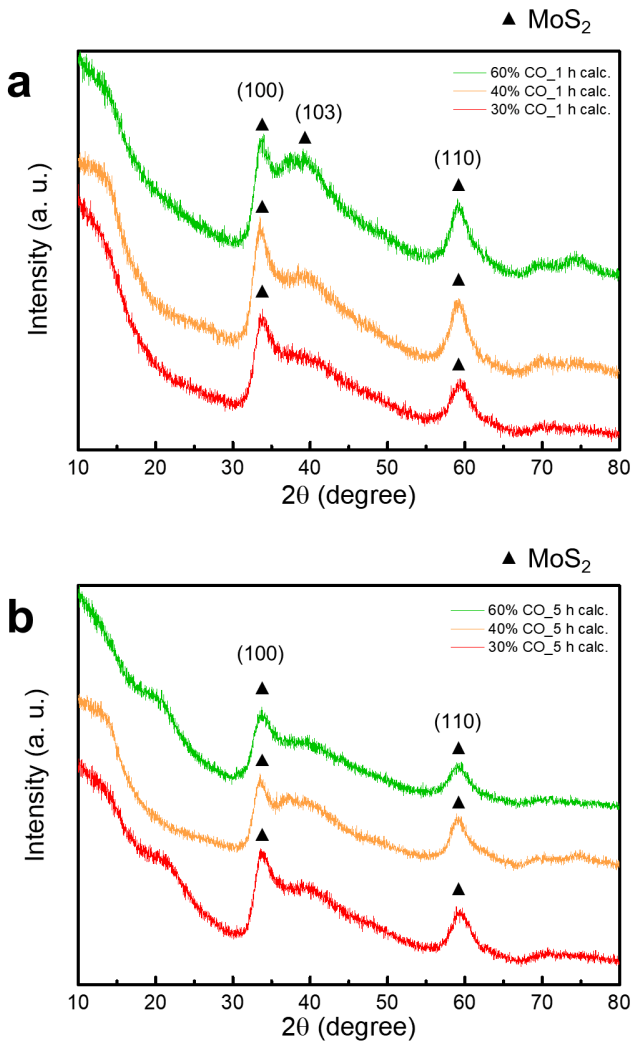

Figure S19. XRD of MoS_2/CNFs was investigated after CO/CO_2 calcination with the isothermal time of (a) 1 h and (b) 5 h. XRD reveals the 1T-MoS_2 (100) and (110) crystallinity in consistent with the XRD pattern of MoS_2 nanosheet structure.[6]

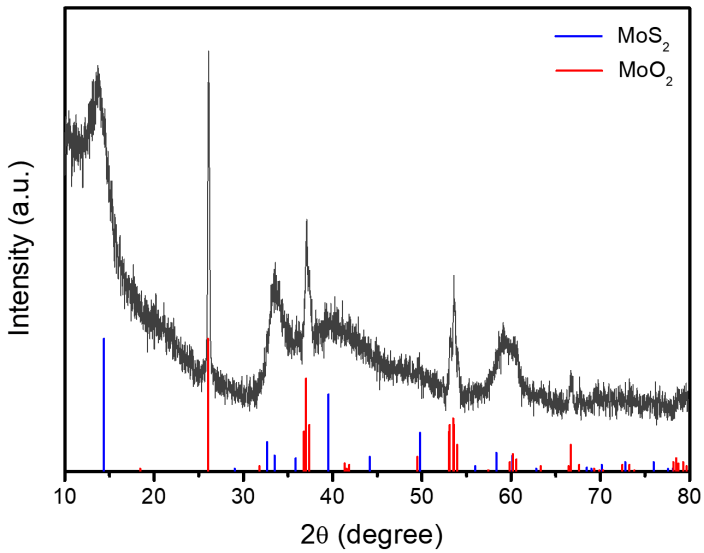

Figure S20. XRD analysis of MoS_2/CNFs after 20% CO ratio calcination. 800 °C calcination at 20% CO ratio condition induced the simultaneous formation of MoS_2 phase and MoO_2 phase. MoO_2 phase at this condition has been predicted by the calculated MoS_2-CO-CO_2 ternary phase diagram. This result reveals that the selective redox reactions between cation and anion can be controlled according to the thermodynamic-calculation guided synthesis information.

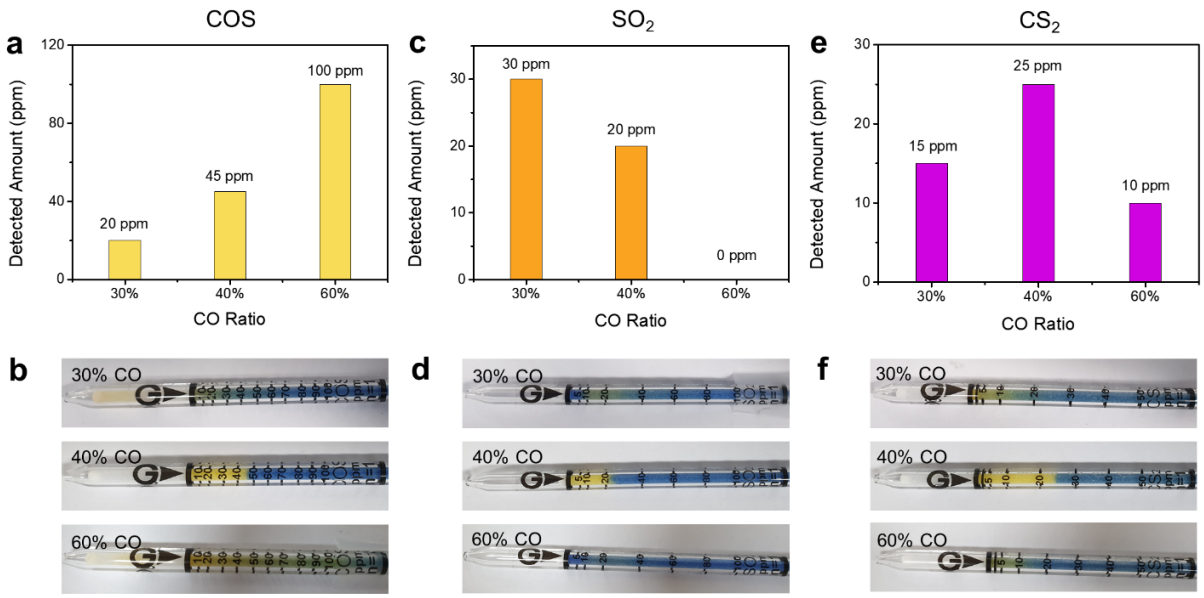

Figure S21. Gas detection during the CO/CO_2 calcination of MoS_2/CNFs. Detected amount comparison and photographs of gas detectors for (a, b) COS, (c, d) SO_2, and (e, f) CS_2 according to the CO ratios of 30%, 40%, and 60%.

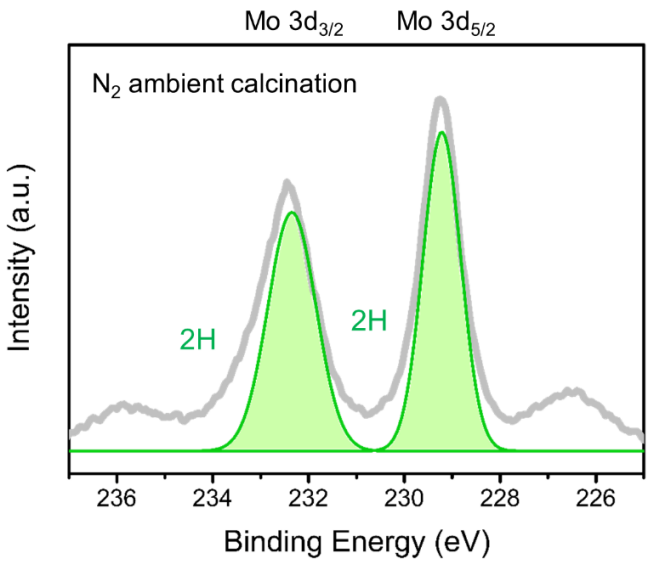

Figure S22. XPS analysis of Mo 3d in MoS_2/CNFs after 800 °C, 5 h calcination under N_2 ambient. Calcination under N_2 does not induce 1T-MoS_2 formation in MoS_2/CNFs.

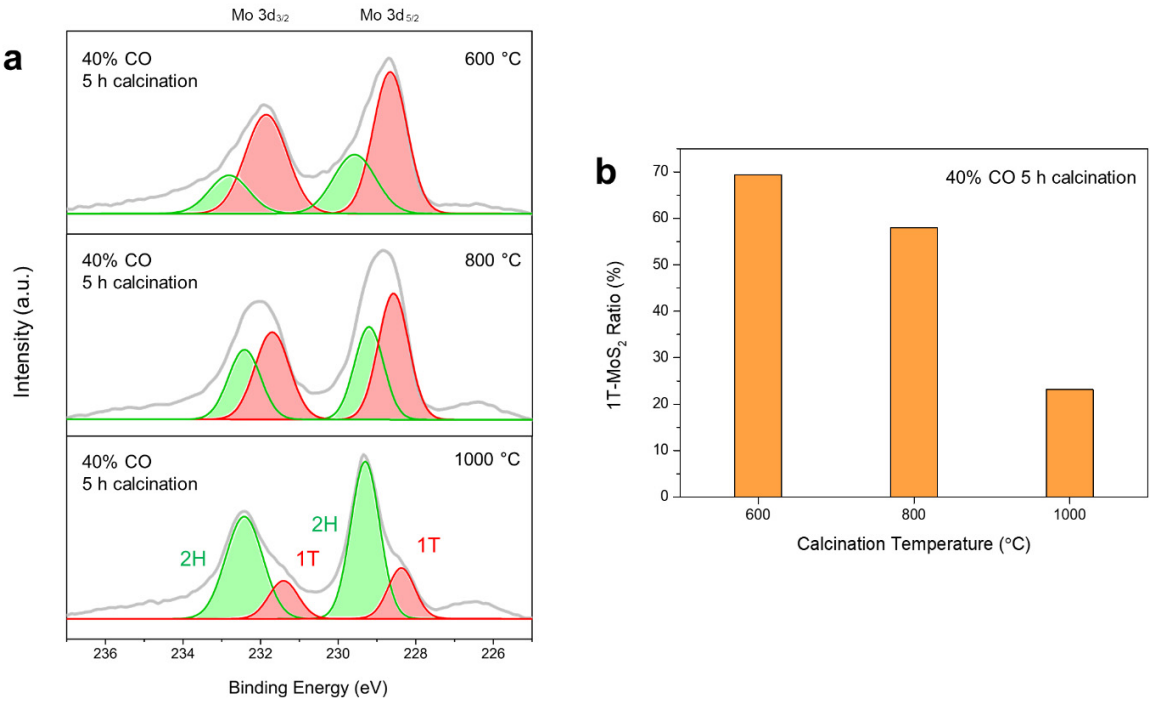

Figure S23. Effect of calcination temperature on 1T-MoS_2 formation. (a) XPS analysis of Mo 3d for determining the polymorph ratio of 2H and 1T-MoS_2 in MoS_2/CNFs according to the temperature (600, 800, 1000 °C) of CO/CO_2 calcination (40% CO and 5 h condition). (b) 1T-MoS_2 ratio in MoS_2/CNFs according to the calcination temperature.

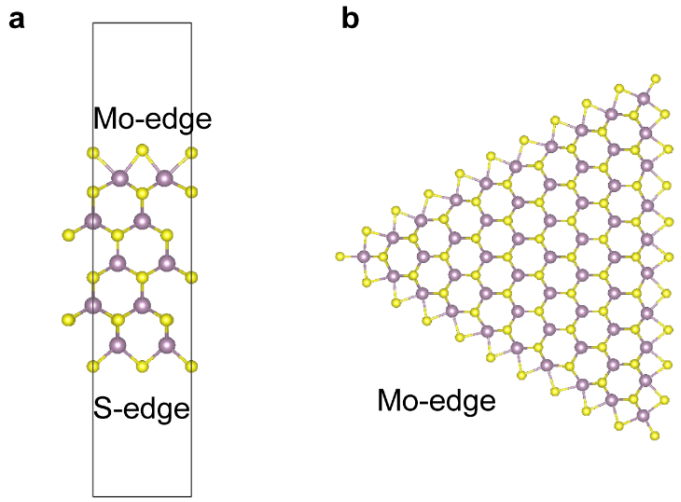

Figure S24. Method to calculate edge energies of MoS_2. (a) Simulation cell for ribbon model which exposes both 50% terminated Mo-edge and S-edge for 2H-MoS_2. (b) 2H-MoS_2 nanoparticle with 50% terminated Mo edge.

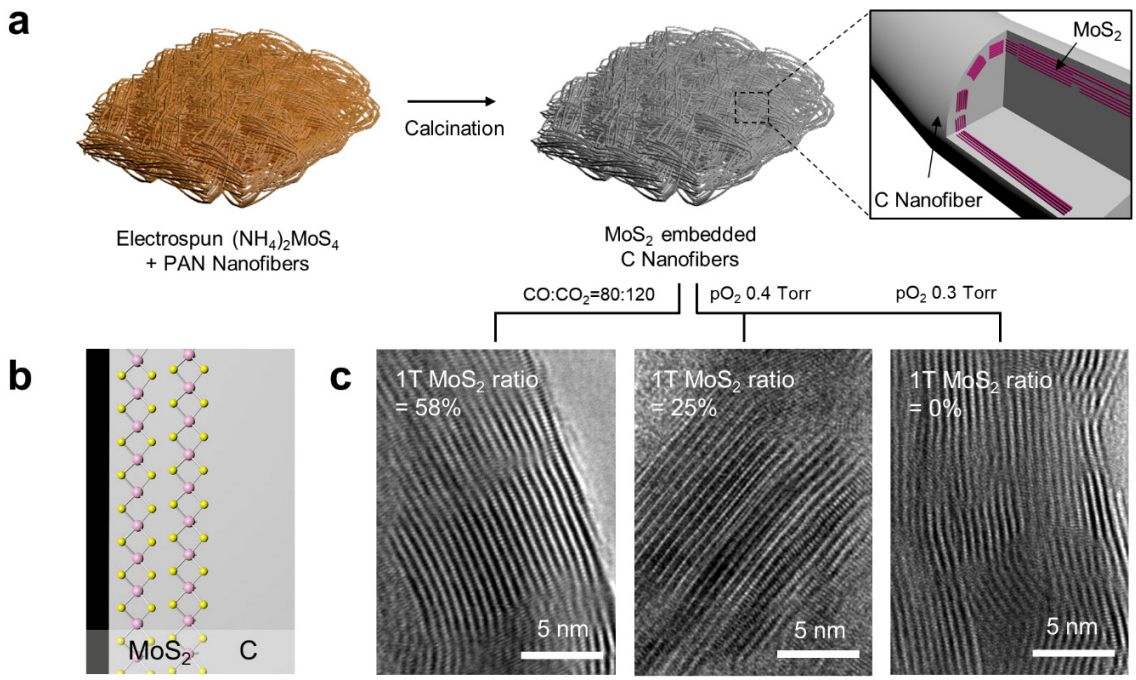

Figure S25. Application of CO/CO_2 calcination on MoS_2/CNFs fabrication. (a) Schematic for free-standing 1T-MoS_2/CNFs nanofibers cloth by one-step calcination. (b) MoS_2 atomic arrangement inside CNFs. (c) Bright-field TEM images for vertically aligned MoS_2 layers according to the 1T phase ratio.

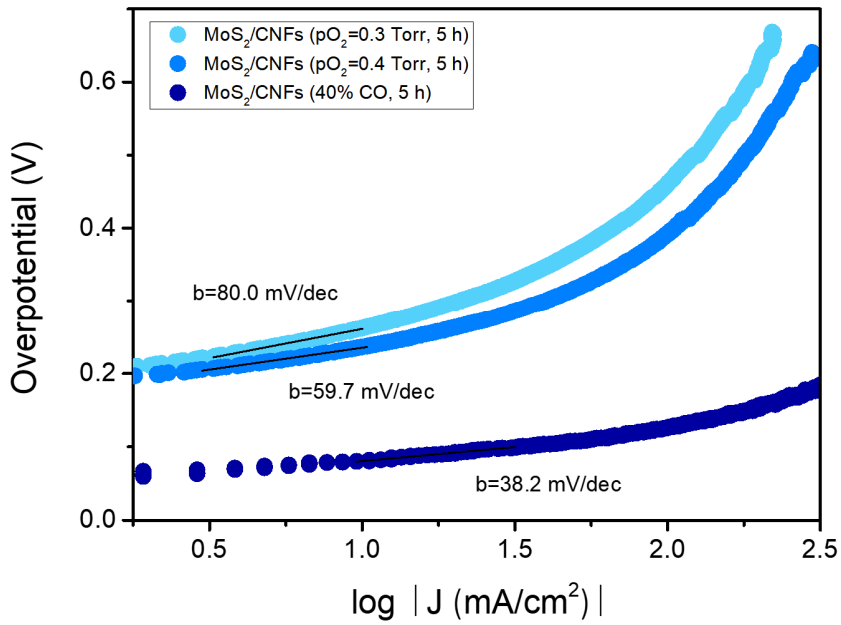

Figure S26. Tafel slope of MoS_2/CNFs. HER Tafel slope comparison of vertically aligned MoS_2/CNFs according to the 1T-MoS_2 ratio.

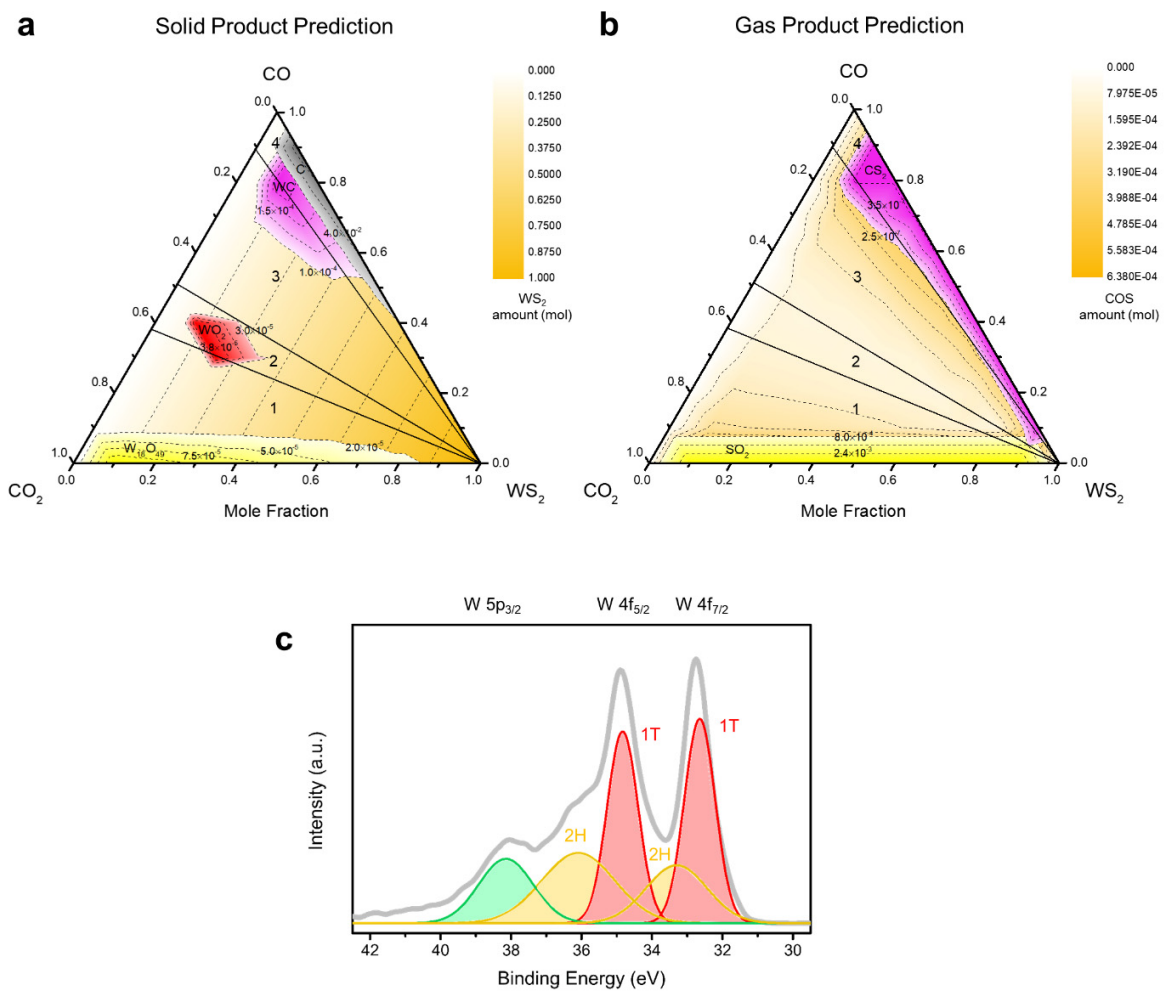

Figure S27. Processing window prediction for WS_2 polymorph conversion. Calculated ternary phase diagrams with (a) solid and (b) gas products at 800 °C calcination to predict WS_2, CO, and CO_2 mole fractions for 1T-WS_2 formation. In the ternary diagram, region 1 displays WS_2 (s) + $W_{18}O_{49}$ (s) + gas; region 2 displays WS_2 (s) + WO_2 (s) + gas; region 3 displays WS_2 (s) + WC (s) + gas; and region 4 displays WS_2 (s) + WC (s) + C (s) + gas. (c) W 4f XPS analysis of WS_2/CNFs which displays the formation of 1T-WS_2 after the 800 °C calcination at 50% CO ratio, which has been predicted in WS_2-CO-CO_2 ternary phase diagram.

Table S1. Cation insertion-based 1T-MoS_2 fabrication methods.[7]

Method	Fabrication condition	Material	Application
Li intercalation[8]	Autoclave 220 ºC for 72 h in n-butyl lithium	1T-MoS_2 on RGO	Photocatalytic H_2 production
Li intercalation[9]	Heated under Ar in n-butyl lithium for 48 h	1T-MoS_2	Supercapacitor
Li intercalation[10]	Heated under Ar at 60 ºC in n-butyl lithium for 48 h	1T-MoS_2	Electrochemical H_2 production
NH_4^+ intercalation[11]	Autoclave 200 ºC for 24 h with $(NH_4)_6Mo_7O_{24}$ + urea	1T-MoS_2	Photocatalytic H_2 production
Li intercalation[12]	MoS_2 heated under Ar at 300 ºC for 3 days in lithium borohydrate	1T-MoS_2	Electrochemical H_2 production
Li intercalation[13]	MoS_2 flake under butyllithium for overnight + e beam lithography	1T'-MoS_2	Electrochemical H_2 production
Sulfur vacancy formation (This work)	**CO/CO_2 calcination for 1~5 h**	**1T-MoS_2**	**Electrochemical H_2 production**

Table S2. Thermodynamic calcination of solid products after calculation according to the CO, CO_2, and MoS_2.

Before reaction (mol)			After reaction (mol)				
MoS_2	CO	CO_2	MoS_2	MoO_2	Mo_2C	MoC	C
0.1	0.1	0.8	1.00E-01	2.19E-05	0.00E+00	0.00E+00	0.00E+00
0.1	0.2	0.7	1.00E-01	1.90E-05	0.00E+00	0.00E+00	0.00E+00
0.1	0.3	0.6	1.00E-01	1.63E-05	0.00E+00	0.00E+00	0.00E+00
0.1	0.4	0.5	1.00E-01	1.36E-05	0.00E+00	0.00E+00	0.00E+00
0.1	0.5	0.4	1.00E-01	0.00E+00	8.29E-06	0.00E+00	0.00E+00
0.1	0.6	0.3	1.00E-01	0.00E+00	1.17E-05	0.00E+00	0.00E+00
0.1	0.7	0.2	1.00E-01	0.00E+00	1.63E-05	0.00E+00	0.00E+00
0.1	0.8	0.1	9.99E-02	0.00E+00	0.00E+00	5.36E-05	2.15E-03
0.2	0.1	0.7	0.19998	1.91E-05	0.00E+00	0.00E+00	0.00E+00
0.2	0.2	0.6	0.19998	1.63E-05	0.00E+00	0.00E+00	0.00E+00
0.2	0.3	0.5	0.19999	1.36E-05	0.00E+00	0.00E+00	0.00E+00
0.2	0.4	0.4	0.19999	0.00E+00	6.11E-06	0.00E+00	0.00E+00
0.2	0.5	0.3	0.19998	0.00E+00	9.18E-06	0.00E+00	0.00E+00
0.2	0.6	0.2	0.19997	0.00E+00	1.34E-05	0.00E+00	0.00E+00
0.2	0.7	0.1	0.19996	0.00E+00	0.00E+00	4.44E-05	0.00E+00
0.3	0.1	0.6	0.29998	1.63E-05	0.00E+00	0.00E+00	0.00E+00
0.3	0.2	0.5	0.29999	1.36E-05	0.00E+00	0.00E+00	0.00E+00
0.3	0.3	0.4	0.29999	1.08E-05	0.00E+00	0.00E+00	0.00E+00
0.3	0.4	0.3	0.29999	0.00E+00	6.79E-06	0.00E+00	0.00E+00
0.3	0.5	0.2	0.29998	0.00E+00	1.05E-05	0.00E+00	0.00E+00
0.3	0.6	0.1	0.29997	0.00E+00	0.00E+00	3.49E-05	0.00E+00

0.4	0.1	0.5	0.39999	1.36E-05	0.00E+00	0.00E+00	0.00E+00
0.4	0.2	0.4	0.39999	1.08E-05	0.00E+00	0.00E+00	0.00E+00
0.4	0.3	0.3	0.39999	0.00E+00	4.58E-06	0.00E+00	0.00E+00
0.4	0.4	0.2	0.39998	0.00E+00	7.81E-06	0.00E+00	0.00E+00
0.4	0.5	0.1	0.39997	0.00E+00	0.00E+00	2.62E-05	0.00E+00
0.5	0.1	0.4	0.49999	1.09E-05	0.00E+00	0.00E+00	0.00E+00
0.5	0.2	0.3	0.49999	8.13E-06	0.00E+00	0.00E+00	0.00E+00
0.5	0.3	0.2	0.49999	0.00E+00	5.31E-06	0.00E+00	0.00E+00
0.5	0.4	0.1	0.49998	0.00E+00	9.72E-06	0.00E+00	0.00E+00
0.6	0.1	0.3	0.59999	8.13E-06	0.00E+00	0.00E+00	0.00E+00
0.6	0.2	0.2	0.59999	0.00E+00	3.06E-06	0.00E+00	0.00E+00
0.6	0.3	0.1	0.59999	0.00E+00	6.68E-06	0.00E+00	0.00E+00
0.7	0.1	0.2	0.69999	5.42E-06	0.00E+00	0.00E+00	0.00E+00
0.7	0.2	0.1	0.69999	0.00E+00	3.91E-06	0.00E+00	0.00E+00
0.8	0.1	0.1	0.8	0.00E+00	1.53E-06	0.00E+00	0.00E+00
0	0	1	0.00E+00	0.00E+00	0.00E+00	0.00E+00	0.00E+00
0	0.1	0.9	0.00E+00	0.00E+00	0.00E+00	0.00E+00	0.00E+00
0	0.2	0.8	0.00E+00	0.00E+00	0.00E+00	0.00E+00	0.00E+00
0	0.3	0.7	0.00E+00	0.00E+00	0.00E+00	0.00E+00	0.00E+00
0	0.4	0.6	0.00E+00	0.00E+00	0.00E+00	0.00E+00	0.00E+00
0	0.5	0.5	0.00E+00	0.00E+00	0.00E+00	0.00E+00	0.00E+00
0	0.6	0.4	0.00E+00	0.00E+00	0.00E+00	0.00E+00	0.00E+00
0	0.7	0.3	0.00E+00	0.00E+00	0.00E+00	0.00E+00	0.00E+00
0	0.8	0.2	0.00E+00	0.00E+00	0.00E+00	0.00E+00	0.00E+00
0	0.9	0.1	0.00E+00	0.00E+00	0.00E+00	0.00E+00	1.25E-02

0	1	0	0.00E+00	0.00E+00	0.00E+00	0.00E+00	0.10223
0.1	0	0.9	9.90E-02	1.00E-03	0.00E+00	0.00E+00	0.00E+00
0.2	0	0.8	0.19911	8.90E-04	0.00E+00	0.00E+00	0.00E+00
0.3	0	0.7	0.29922	7.78E-04	0.00E+00	0.00E+00	0.00E+00
0.4	0	0.6	3.99E-01	6.67E-04	0.00E+00	0.00E+00	0.00E+00
0.5	0	0.5	0.49944	5.56E-04	0.00E+00	0.00E+00	0.00E+00
0.6	0	0.4	0.59956	4.45E-04	0.00E+00	0.00E+00	0.00E+00
0.7	0	0.3	0.69967	3.34E-04	0.00E+00	0.00E+00	0.00E+00
0.8	0	0.2	0.79978	2.22E-04	0.00E+00	0.00E+00	0.00E+00
0.9	0	0.1	0.89989	1.11E-04	0.00E+00	0.00E+00	0.00E+00
0.1	0.9	0	1.00E-01	0.00E+00	0.00E+00	4.82E-05	9.19E-02
0.2	0.8	0	0.19996	0.00E+00	0.00E+00	4.29E-05	8.17E-02
0.3	0.7	0	0.29996	0.00E+00	0.00E+00	3.75E-05	7.15E-02
0.4	0.6	0	0.39997	0.00E+00	0.00E+00	3.21E-05	6.13E-02
0.5	0.5	0	0.49997	0.00E+00	0.00E+00	2.68E-05	5.11E-02
0.6	0.4	0	0.59998	0.00E+00	0.00E+00	2.14E-05	4.09E-02
0.7	0.3	0	0.69998	0.00E+00	0.00E+00	1.61E-05	3.06E-02
0.8	0.2	0	0.79999	0.00E+00	0.00E+00	1.07E-05	2.04E-02
0.9	0.1	0	0.89999	0.00E+00	0.00E+00	5.36E-06	1.02E-02
1	0	0	1	0	0.00E+00	0.00E+00	0.00E+00

Table S3. Thermodynamic calcination of gas products after calculation according to the relative amount of CO, CO_2, and MoS_2.

Before reaction (mol)			After reaction (mol)			
MoS_2	CO	CO_2	COS	SO_2	S_2	CS_2
0.1	0.1	0.8	4.81E-05	2.96E-07	4.22E-08	6.60E-10
0.1	0.2	0.7	4.21E-05	2.48E-08	8.08E-09	5.77E-10
0.1	0.3	0.6	3.61E-05	4.63E-09	2.64E-09	4.95E-10
0.1	0.4	0.5	3.01E-05	1.13E-09	1.03E-09	4.12E-10
0.1	0.5	0.4	4.02E-05	4.96E-10	1.18E-09	9.24E-10
0.1	0.6	0.3	5.68E-05	2.28E-10	1.64E-09	2.46E-09
0.1	0.7	0.2	7.93E-05	8.90E-11	2.34E-09	7.17E-09
0.1	0.8	0.1	1.19E-04	2.39E-11	4.07E-09	3.15E-08
0.2	0.1	0.7	4.73E-05	1.98E-07	3.23E-08	6.50E-10
0.2	0.2	0.6	4.06E-05	1.56E-08	5.93E-09	5.57E-10
0.2	0.3	0.5	3.38E-05	2.68E-09	1.83E-09	4.64E-10
0.2	0.4	0.4	3.34E-05	7.14E-10	1.00E-09	5.64E-10
0.2	0.5	0.3	5.01E-05	3.09E-10	1.45E-09	1.70E-09
0.2	0.6	0.2	7.29E-05	1.16E-10	2.13E-09	5.39E-09
0.2	0.7	0.1	1.11E-04	2.77E-11	3.62E-09	2.49E-08
0.3	0.1	0.6	4.64E-05	1.25E-07	2.37E-08	6.36E-10
0.3	0.2	0.5	3.86E-05	9.04E-09	4.12E-09	5.30E-10
0.3	0.3	0.4	3.09E-05	1.37E-09	1.17E-09	4.24E-10
0.3	0.4	0.3	4.24E-05	4.46E-10	1.24E-09	1.06E-09
0.3	0.5	0.2	6.55E-05	1.57E-10	1.89E-09	3.81E-09
0.3	0.6	0.1	1.02E-04	3.55E-11	3.22E-09	1.86E-08

0.4	0.1	0.5	4.51E-05	7.23E-08	1.65E-08	6.19E-10
0.4	0.2	0.4	3.61E-05	4.63E-09	2.64E-09	4.95E-10
0.4	0.3	0.3	3.34E-05	7.14E-10	1.00E-09	5.64E-10
0.4	0.4	0.2	5.68E-05	2.28E-10	1.64E-09	2.46E-09
0.4	0.5	0.1	9.44E-05	4.85E-11	2.89E-09	1.36E-08
0.5	0.1	0.4	4.33E-05	3.70E-08	1.06E-08	5.94E-10
0.5	0.2	0.3	3.25E-05	1.95E-09	1.48E-09	4.45E-10
0.5	0.3	0.2	4.64E-05	3.67E-10	1.35E-09	1.36E-09
0.5	0.4	0.1	8.49E-05	7.10E-11	2.54E-09	9.13E-09
0.6	0.1	0.3	4.06E-05	1.56E-08	5.93E-09	5.57E-10
0.6	0.2	0.2	3.34E-05	7.14E-10	1.00E-09	5.64E-10
0.6	0.3	0.1	7.29E-05	1.16E-10	2.13E-09	5.39E-09
0.7	0.1	0.2	3.61E-05	4.63E-09	2.64E-09	4.95E-10
0.7	0.2	0.1	5.68E-05	2.28E-10	1.64E-09	2.46E-09
0.8	0.1	0.1	3.34E-05	7.14E-10	1.00E-09	5.64E-10
0	0	1	0.00E+00	0.00E+00	0.00E+00	0.00E+00
0	0.1	0.9	0.00E+00	0.00E+00	0.00E+00	0.00E+00
0	0.2	0.8	0.00E+00	0.00E+00	0.00E+00	0.00E+00
0	0.3	0.7	0.00E+00	0.00E+00	0.00E+00	0.00E+00
0	0.4	0.6	0.00E+00	0.00E+00	0.00E+00	0.00E+00
0	0.5	0.5	0.00E+00	0.00E+00	0.00E+00	0.00E+00
0	0.6	0.4	0.00E+00	0.00E+00	0.00E+00	0.00E+00
0	0.7	0.3	0.00E+00	0.00E+00	0.00E+00	0.00E+00
0	0.8	0.2	0.00E+00	0.00E+00	0.00E+00	0.00E+00
0	0.9	0.1	0.00E+00	0.00E+00	0.00E+00	0.00E+00

0	1	0	0.00E+00	0.00E+00	0.00E+00	0.00E+00
0.1	0	0.9	5.36E-05	2.13E-03	1.57E-05	7.36E-10
0.2	0	0.8	5.36E-05	2.13E-03	1.57E-05	7.36E-10
0.3	0	0.7	5.36E-05	2.13E-03	1.57E-05	7.36E-10
0.4	0	0.6	5.36E-05	2.13E-03	1.57E-05	7.36E-10
0.5	0	0.5	5.36E-05	2.13E-03	1.57E-05	7.36E-10
0.6	0	0.4	5.36E-05	2.13E-03	1.57E-05	7.36E-10
0.7	0	0.3	5.36E-05	2.13E-03	1.57E-05	7.36E-10
0.8	0	0.2	5.36E-05	2.13E-03	1.57E-05	7.36E-10
0.9	0	0.1	5.36E-05	2.13E-03	1.57E-05	7.36E-10
0.1	0.9	0	1.19E-04	2.39E-11	4.07E-09	3.15E-08
0.2	0.8	0	1.19E-04	2.39E-11	4.07E-09	3.15E-08
0.3	0.7	0	1.19E-04	2.39E-11	4.07E-09	3.15E-08
0.4	0.6	0	1.19E-04	2.39E-11	4.07E-09	3.15E-08
0.5	0.5	0	1.19E-04	2.39E-11	4.07E-09	3.15E-08
0.6	0.4	0	1.19E-04	2.39E-11	4.07E-09	3.15E-08
0.7	0.3	0	1.19E-04	2.39E-11	4.07E-09	3.15E-08
0.8	0.2	0	1.19E-04	2.39E-11	4.07E-09	3.15E-08
0.9	0.1	0	1.19E-04	2.39E-11	4.07E-09	3.15E-08
1	0	0	0.00E+00	0.00E+00	2.16E-10	0.00E+00

Table S4. Mo-S atomic distance, Mo-S coordination number of MoS_2, and fitting parameters in MoS_2/CNFs extracted by fitting EXAFS.

Condition	Mo-S atomic distance (Å)	Mo-S coordination number	σ^2	ΔE_0
30% CO, 1 h	2.4	5.15 ± 0.44	0.0029	-0.96
60% CO, 1 h	2.4	4.65 ± 0.40	0.0030	-1.12
25% CO, 5 h	2.4	5.29 ± 0.44	0.0025	2.48
30% CO, 5 h	2.4	4.72 ± 0.36	0.0028	3.13
40% CO, 5 h	2.4	4.00 ± 0.27	0.0028	3.02
60% CO, 5 h	2.4	3.86 ± 0.39	0.0030	3.64

Table S5. Edge energy of 50% terminated Mo-edge in nanoparticle as a function of particle size.

Particle size (number of Mo at one edge)	E_{edge} (eV/Å)
4	0.59
6	0.61
8	0.61
10	0.60

Table S6. Vacancy formation energies (E_f) of edges at 2H-MoS_2 and 1T′-MoS_2.

	2H phase		1T' phase	
	Mo-edge	S-edge	Edge 1	Edge 2
E_f (eV)	0.70	0.25	0.26	0.79

Table S7. MoS_2 based HER electrocatalyst performance comparison.

Strategy	Catalyst	Electrolyte	Tafel slope (mV/dec)	E at 10 mA/cm^2 (mV)
This work	Phase and structure modulated 1T-MoS_2/CNFs	0.5M H_2SO_4	38.2	80.5
Increase edge active site	Double gyroid porous MoS_2[14]	0.5M H_2SO_4	50	230
	Defect rich ultrathin MoS_2 nanosheet[15]	0.5M H_2SO_4	50	190
	MoS_2 nanobelts[16]	0.5M H_2SO_4	70	140
	MoS_2 monolayer[17]	0.5M H_2SO_4	61	210
	MoS_2 nanoparticle[18]	0.5M H_2SO_4	69	220
	Stepped Edge surface terminated MoS_2[19]	0.5M H_2SO_4	59	104
	MoS_2 nanoplates[20]	0.5M H_2SO_4	53	160
	MoS_2 nano-assembled sphere[21]	0.5M H_2SO_4	100	200
Increase defect density on the basal plane	Defective O-doped MoS_2 nanosheet[22]	0.5M H_2SO_4	55	180
	Strained 2H monolayer[23]	0.5M H_2SO_4	60	170
	Plasma treated MoS_2 thin film[24]	0.5M H_2SO_4	105	300
	MoS_2 with sulfur vacancy[25]	0.5M H_2SO_4	70	170
Tuning the electronic structure and phase	1T-MoS_2 nanosheets[10]	0.5M H_2SO_4	43	187
	lithiated MoS_2 vertical layers[26]	0.5M H_2SO_4	44	168
	Porous 1T-MoS_2 nanosheets[27]	0.5M H_2SO_4	43	153
	Li intercalated 1T-MoS_2 + CNF[28]	0.5M H_2SO_4	62	118
	1T-MoS_2 nanosheets[12]	0.5M H_2SO_4	40	200
	1T-MoS_2 nanodot[29]	0.5M H_2SO_4	40	140
	1T-MoS_2 flake on graphite[30]	0.5M H_2SO_4	51	250
Coupling with conductive scaffolds	MoS_2/RGO hybrid[31]	0.5M H_2SO_4	41	150
	MoS_2/CNT hybrid[32]	0.5M H_2SO_4	44.6	180
	MoS_2/N doped CNT hybrid[33]	0.5M H_2SO_4	40	110
	MoS_2/ordered mesoporous carbon[34]	0.5M H_2SO_4	60	182
	Edge terminated MoS_2 in 3D Carbon[1]	0.5M H_2SO_4	46.2	110
Amorphous	amorphous MoSx[35]	0.5M H_2SO_4	46	160

Table S8. Thermodynamic calcination of solid products after calculation according to the CO, CO_2, and WS_2.

Before reaction (mol)			After reaction (mol)				
WS_2	CO	CO_2	WS_2	$W_{18}O_{49}$	WO_2	WC	C
0.1	0.1	0.8	9.99E-02	6.45E-06	0.00E+00	0.00E+00	0.00E+00
0.1	0.2	0.7	9.99E-02	4.13E-06	0.00E+00	0.00E+00	0.00E+00
0.1	0.3	0.6	9.99E-02	2.89E-06	0.00E+00	0.00E+00	0.00E+00
0.1	0.4	0.5	1.00E-01	0.00E+00	4.06E-05	0.00E+00	0.00E+00
0.1	0.5	0.4	1.00E-01	0.00E+00	0.00E+00	3.83E-05	0.00E+00
0.1	0.6	0.3	9.99E-02	0.00E+00	0.00E+00	6.37E-05	0.00E+00
0.1	0.7	0.2	9.99E-02	0.00E+00	0.00E+00	1.06E-04	0.00E+00
0.1	0.8	0.1	9.98E-02	0.00E+00	0.00E+00	1.93E-04	1.98E-03
0.2	0.1	0.7	2.00E-01	5.35E-06	0.00E+00	0.00E+00	0.00E+00
0.2	0.2	0.6	2.00E-01	3.35E-06	0.00E+00	0.00E+00	0.00E+00
0.2	0.3	0.5	2.00E-01	0.00E+00	4.06E-05	0.00E+00	0.00E+00
0.2	0.4	0.4	2.00E-01	0.00E+00	3.25E-05	0.00E+00	0.00E+00
0.2	0.5	0.3	2.00E-01	0.00E+00	0.00E+00	4.69E-05	0.00E+00
0.2	0.6	0.2	2.00E-01	0.00E+00	0.00E+00	8.28E-05	0.00E+00
0.2	0.7	0.1	2.00E-01	0.00E+00	0.00E+00	1.59E-04	0.00E+00
0.3	0.1	0.6	3.00E-01	4.32E-06	0.00E+00	0.00E+00	0.00E+00
0.3	0.2	0.5	3.00E-01	2.61E-06	0.00E+00	0.00E+00	0.00E+00
0.3	0.3	0.4	3.00E-01	0.00E+00	3.25E-05	0.00E+00	0.00E+00
0.3	0.4	0.3	3.00E-01	0.00E+00	0.00E+00	3.21E-05	0.00E+00
0.3	0.5	0.2	3.00E-01	0.00E+00	0.00E+00	6.15E-05	0.00E+00
0.3	0.6	0.1	3.00E-01	0.00E+00	0.00E+00	1.25E-04	0.00E+00

0.4	0.1	0.5	4.00E-01	3.37E-06	0.00E+00	0.00E+00	0.00E+00
0.4	0.2	0.4	4.00E-01	1.93E-06	0.00E+00	0.00E+00	0.00E+00
0.4	0.3	0.3	4.00E-01	0.00E+00	2.44E-05	0.00E+00	0.00E+00
0.4	0.4	0.2	4.00E-01	0.00E+00	0.00E+00	4.25E-05	0.00E+00
0.4	0.5	0.1	4.00E-01	0.00E+00	0.00E+00	9.39E-05	0.00E+00
0.5	0.1	0.4	5.00E-01	2.48E-06	0.00E+00	0.00E+00	0.00E+00
0.5	0.2	0.3	5.00E-01	0.00E+00	2.44E-05	0.00E+00	0.00E+00
0.5	0.3	0.2	5.00E-01	0.00E+00	0.00E+00	2.62E-05	0.00E+00
0.5	0.4	0.1	5.00E-01	0.00E+00	0.00E+00	6.58E-05	0.00E+00
0.6	0.1	0.3	6.00E-01	1.67E-06	0.00E+00	0.00E+00	0.00E+00
0.6	0.2	0.2	6.00E-01	0.00E+00	1.62E-05	0.00E+00	0.00E+00
0.6	0.3	0.1	6.00E-01	0.00E+00	0.00E+00	4.14E-05	0.00E+00
0.7	0.1	0.2	7.00E-01	9.63E-07	0.00E+00	0.00E+00	0.00E+00
0.7	0.2	0.1	7.00E-01	0.00E+00	0.00E+00	2.12E-05	0.00E+00
0.8	0.1	0.1	8.00E-01	0.00E+00	8.12E-06	0.00E+00	0.00E+00
0	0	1	0.00E+00	0.00E+00	0.00E+00	0.00E+00	0.00E+00
0	0.1	0.9	0.00E+00	0.00E+00	0.00E+00	0.00E+00	0.00E+00
0	0.2	0.8	0.00E+00	0.00E+00	0.00E+00	0.00E+00	0.00E+00
0	0.3	0.7	0.00E+00	0.00E+00	0.00E+00	0.00E+00	0.00E+00
0	0.4	0.6	0.00E+00	0.00E+00	0.00E+00	0.00E+00	0.00E+00
0	0.5	0.5	0.00E+00	0.00E+00	0.00E+00	0.00E+00	0.00E+00
0	0.6	0.4	0.00E+00	0.00E+00	0.00E+00	0.00E+00	0.00E+00
0	0.7	0.3	0.00E+00	0.00E+00	0.00E+00	0.00E+00	0.00E+00
0	0.8	0.2	0.00E+00	0.00E+00	0.00E+00	0.00E+00	0.00E+00
0	0.9	0.1	0.00E+00	0.00E+00	0.00E+00	0.00E+00	0.00E+00

0	1	0	0.00E+00	0.00E+00	0.00E+00	0.00E+00	0.00E+00
0.1	0	0.9	9.77E-02	1.26E-04	0.00E+00	0.00E+00	0.00E+00
0.2	0	0.8	1.98E-01	1.12E-04	0.00E+00	0.00E+00	0.00E+00
0.3	0	0.7	2.98E-01	9.83E-05	0.00E+00	0.00E+00	0.00E+00
0.4	0	0.6	3.98E-01	8.43E-05	0.00E+00	0.00E+00	0.00E+00
0.5	0	0.5	4.99E-01	7.02E-05	0.00E+00	0.00E+00	0.00E+00
0.6	0	0.4	5.99E-01	5.62E-05	0.00E+00	0.00E+00	0.00E+00
0.7	0	0.3	6.99E-01	4.21E-05	0.00E+00	0.00E+00	0.00E+00
0.8	0	0.2	7.99E-01	2.81E-05	0.00E+00	0.00E+00	0.00E+00
0.9	0	0.1	9.00E-01	1.40E-05	0.00E+00	0.00E+00	0.00E+00
0.1	0.9	0	9.98E-02	0.00E+00	0.00E+00	1.73E-04	9.18E-02
0.2	0.8	0	2.00E-01	0.00E+00	0.00E+00	1.54E-04	8.16E-02
0.3	0.7	0	3.00E-01	0.00E+00	0.00E+00	1.35E-04	7.14E-02
0.4	0.6	0	4.00E-01	0.00E+00	0.00E+00	1.16E-04	6.12E-02
0.5	0.5	0	5.00E-01	0.00E+00	0.00E+00	9.63E-05	5.10E-02
0.6	0.4	0	6.00E-01	0.00E+00	0.00E+00	7.71E-05	4.08E-02
0.7	0.3	0	7.00E-01	0.00E+00	0.00E+00	5.78E-05	3.06E-02
0.8	0.2	0	8.00E-01	0.00E+00	0.00E+00	3.85E-05	2.04E-02
0.9	0.1	0	9.00E-01	0.00E+00	0.00E+00	1.93E-05	1.02E-02
1	0	0	1.00E+00	0.00E+00	0.00E+00	0.00E+00	0.00E+00

Table S9. Thermodynamic calcination of gas products after calculation according to the CO, CO_2, and WS_2.

Before reaction (mol)			After reaction (mol)			
WS_2	CO	CO_2	COS	SO_2	S_2	CS_2
0.1	0.1	0.8	2.54E-04	1.57E-06	1.18E-06	1.84E-08
0.1	0.2	0.7	1.65E-04	9.75E-08	1.24E-07	8.87E-09
0.1	0.3	0.6	1.15E-04	1.49E-08	2.71E-08	5.07E-09
0.1	0.4	0.5	9.02E-05	3.41E-09	9.30E-09	3.71E-09
0.1	0.5	0.4	8.52E-05	1.06E-09	5.31E-09	4.14E-09
0.1	0.6	0.3	1.42E-04	5.71E-10	1.02E-08	1.52E-08
0.1	0.7	0.2	2.36E-04	2.67E-10	2.08E-08	6.35E-08
0.1	0.8	0.1	4.28E-04	8.57E-11	5.28E-08	4.09E-07
0.2	0.1	0.7	2.38E-04	1.00E-06	8.19E-07	1.64E-08
0.2	0.2	0.6	1.50E-04	5.81E-08	8.17E-08	7.65E-09
0.2	0.3	0.5	1.01E-04	8.07E-09	1.65E-08	4.18E-09
0.2	0.4	0.4	8.12E-05	1.74E-09	5.95E-09	3.34E-09
0.2	0.5	0.3	1.17E-04	7.27E-10	7.97E-09	9.31E-09
0.2	0.6	0.2	2.07E-04	3.30E-10	1.72E-08	4.34E-08
0.2	0.7	0.1	3.98E-04	1.00E-10	4.67E-08	3.20E-07
0.3	0.1	0.6	2.21E-04	5.96E-07	5.39E-07	1.44E-08
0.3	0.2	0.5	1.34E-04	3.15E-08	4.97E-08	6.39E-09
0.3	0.3	0.4	9.28E-05	4.13E-09	1.06E-08	3.82E-09
0.3	0.4	0.3	9.18E-05	9.72E-10	5.83E-09	4.98E-09
0.3	0.5	0.2	1.76E-04	4.23E-10	1.37E-08	2.73E-08
0.3	0.6	0.1	3.57E-04	1.25E-10	3.93E-08	2.26E-07

0.4	0.1	0.5	2.01E-04	3.23E-07	3.28E-07	1.23E-08
0.4	0.2	0.4	1.15E-04	1.49E-08	2.71E-08	5.07E-09
0.4	0.3	0.3	8.12E-05	1.74E-09	5.95E-09	3.34E-09
0.4	0.4	0.2	1.42E-04	5.71E-10	1.02E-08	1.52E-08
0.4	0.5	0.1	3.13E-04	1.62E-10	3.18E-08	1.49E-07
0.5	0.1	0.4	1.78E-04	1.53E-07	1.79E-07	1.00E-08
0.5	0.2	0.3	9.74E-05	5.88E-09	1.34E-08	4.01E-09
0.5	0.3	0.2	1.05E-04	8.34E-10	6.88E-09	6.95E-09
0.5	0.4	0.1	2.63E-04	2.22E-10	2.45E-08	8.77E-08
0.6	0.1	0.3	1.50E-04	5.81E-08	8.17E-08	7.65E-09
0.6	0.2	0.2	8.12E-05	1.74E-09	5.95E-09	3.34E-09
0.6	0.3	0.1	2.07E-04	3.30E-10	1.72E-08	4.34E-08
0.7	0.1	0.2	1.15E-04	1.49E-08	2.71E-08	5.07E-09
0.7	0.2	0.1	1.42E-04	5.71E-10	1.02E-08	1.52E-08
0.8	0.1	0.1	8.12E-05	1.74E-09	5.95E-09	3.34E-09
0	0	1	0.00E+00	0.00E+00	0.00E+00	0.00E+00
0	0.1	0.9	0.00E+00	0.00E+00	0.00E+00	0.00E+00
0	0.2	0.8	0.00E+00	0.00E+00	0.00E+00	0.00E+00
0	0.3	0.7	0.00E+00	0.00E+00	0.00E+00	0.00E+00
0	0.4	0.6	0.00E+00	0.00E+00	0.00E+00	0.00E+00
0	0.5	0.5	0.00E+00	0.00E+00	0.00E+00	0.00E+00
0	0.6	0.4	0.00E+00	0.00E+00	0.00E+00	0.00E+00
0	0.7	0.3	0.00E+00	0.00E+00	0.00E+00	0.00E+00
0	0.8	0.2	0.00E+00	0.00E+00	0.00E+00	0.00E+00
0	0.9	0.1	0.00E+00	0.00E+00	0.00E+00	0.00E+00

0	1	0	0.00E+00	0.00E+00	0.00E+00	0.00E+00
0.1	0	0.9	6.38E-04	3.23E-03	5.70E-04	1.05E-07
0.2	0	0.8	6.38E-04	3.23E-03	5.70E-04	1.05E-07
0.3	0	0.7	6.38E-04	3.23E-03	5.70E-04	1.05E-07
0.4	0	0.6	6.38E-04	3.23E-03	5.70E-04	1.05E-07
0.5	0	0.5	6.38E-04	3.23E-03	5.70E-04	1.05E-07
0.6	0	0.4	6.38E-04	3.23E-03	5.70E-04	1.05E-07
0.7	0	0.3	6.38E-04	3.23E-03	5.70E-04	1.05E-07
0.8	0	0.2	6.38E-04	3.23E-03	5.70E-04	1.05E-07
0.9	0	0.1	6.38E-04	3.23E-03	5.70E-04	1.05E-07
0.1	0.9	0	4.28E-04	8.57E-11	5.28E-08	4.09E-07
0.2	0.8	0	4.28E-04	8.57E-11	5.28E-08	4.09E-07
0.3	0.7	0	4.28E-04	8.57E-11	5.28E-08	4.09E-07
0.4	0.6	0	4.28E-04	8.57E-11	5.28E-08	4.09E-07
0.5	0.5	0	4.28E-04	8.57E-11	5.28E-08	4.09E-07
0.6	0.4	0	4.28E-04	8.57E-11	5.28E-08	4.09E-07
0.7	0.3	0	4.28E-04	8.57E-11	5.28E-08	4.09E-07
0.8	0.2	0	4.28E-04	8.57E-11	5.28E-08	4.09E-07
0.9	0.1	0	4.28E-04	8.57E-11	5.28E-08	4.09E-07
1	0	0	0.00E+00	0.00E+00	0.00E+00	0.00E+00

REFERENCES

(1) Chung, D. Y.; Yoo, J. M.; Park, S.; Jung, G. Y.; Kang, J. S.; Ahn, C.-Y.; Kwak, S. K.; Sung, Y.-E. *Small* **2018**, *14*, 1802191.

(2) Yuqiang, F.; Jie, P.; Jianqiao, H.; Ruichun, L.; Dong, W.; Xiangli, C.; Kejun, B.; Wei, Z.; Pan, L.; Gang, M.; et al. *Angew. Chemie* **2018**, *130*, 1246–1249.

(3) Hinnemann, B.; Moses, P. G.; Bonde, J.; Jørgensen, K. P.; Nielsen, J. H.; Horch, S.; Chorkendorff, I.; Nørskov, J. K. *J. Am. Chem. Soc.* **2005**, *127*, 5308–5309.

(4) Bollinger, M. V; Jacobsen, K. W.; Nørskov, J. K. *Phys. Rev. B* **2003**, *67*, 85410.

(5) Mortazavi, M.; Wang, C.; Deng, J.; Shenoy, V. B.; Medhekar, N. V. *J. Power Sources* **2014**, *268*, 279–286.

(6) Yang, L.; Cui, X.; Zhang, J.; Wang, K.; Shen, M.; Zeng, S.; Dayeh, S. A.; Feng, L.; Xiang, B. *Sci. Rep.* **2014**, *4*, 5649.

(7) Lei, Z.; Zhan, J.; Tang, L.; Zhang, Y.; Wang, Y. *Adv. Energy Mater.* **2018**, *8*, 1703482.

(8) Maitra, U.; Gupta, U.; De, M.; Datta, R.; Govindaraj, A.; Rao, C. N. R. *Angew. Chemie* **2013**, *125*, 13295–13299.

(9) Acerce, M.; Voiry, D.; Chhowalla, M. *Nat. Nanotechnol.* **2015**, *10*, 313–318.

(10) Lukowski, M. A.; Daniel, A. S.; Meng, F.; Forticaux, A.; Li, L.; Jin, S. *J. Am. Chem. Soc.* **2013**, *135*, 10274–10277.

(11) Liu, Q.; Li, X.; He, Q.; Khalil, A.; Liu, D.; Xiang, T.; Wu, X.; Song, L. *Small* **2015**, *11*, 5556–5564.

(12) Voiry, D.; Salehi, M.; Silva, R.; Fujita, T.; Chen, M.; Asefa, T.; Shenoy, V. B.; Eda, G.; Chhowalla, M. *Nano Lett.* **2013**, *13*, 6222–6227.

(13) Zhang, J.; Wu, J.; Guo, H.; Chen, W.; Yuan, J.; Martinez, U.; Gupta, G.; Mohite, A.; Ajayan, P. M.; Lou, J. *Adv. Mater.* **2017**, *29*, 1701955.

(14) Kibsgaard, J.; Chen, Z.; Reinecke, B. N.; Jaramillo, T. F. *Nat. Mater.* **2012**, *11*, 963–969.

(15) Xie, J.; Zhang, H.; Li, S.; Wang, R.; Sun, X.; Zhou, M.; Zhou, J.; Lou, X. W. (David); Xie, Y. *Adv. Mater.* **2013**, *25*, 5807–5813.

(16) Yang, L.; Hong, H.; Fu, Q.; Huang, Y.; Zhang, J.; Cui, X.; Fan, Z.; Liu, K.; Xiang, B. *ACS Nano* **2015**, *9*, 6478–6483.

(17) Shi, J.; Ma, D.; Han, G.-F.; Zhang, Y.; Ji, Q.; Gao, T.; Sun, J.; Song, X.; Li, C.; Zhang, Y.; et al. *ACS Nano* **2014**, *8*, 10196–10204.

(18) Wang, T.; Liu, L.; Zhu, Z.; Papakonstantinou, P.; Hu, J.; Liu, H.; Li, M. *Energy Environ. Sci.* **2013**, *6*, 625–633.

(19) Hu, J.; Huang, B.; Zhang, C.; Wang, Z.; An, Y.; Zhou, D.; Lin, H.; Leung, M. K. H.; Yang, S. *Energy Environ. Sci.* **2017**, *10*, 593–603.

(20) Yan, Y.; Xia, B.; Ge, X.; Liu, Z.; Wang, J.-Y.; Wang, X. *ACS Appl. Mater. Interfaces* **2013**, *5*, 12794–12798.

(21) Chung, D. Y.; Park, S.-K.; Chung, Y.-H.; Yu, S.-H.; Lim, D.-H.; Jung, N.; Ham, H. C.; Park, H.-Y.; Piao, Y.; Yoo, S. J.; et al. *Nanoscale* **2014**, *6*, 2131–2136.

(22) Xie, J.; Zhang, J.; Li, S.; Grote, F.; Zhang, X.; Zhang, H.; Wang, R.; Lei, Y.; Pan, B.; Xie, Y. *J. Am. Chem. Soc.* **2013**, *135*, 17881–17888.

(23) Li, H.; Tsai, C.; Koh, A. L.; Cai, L.; Contryman, A. W.; Fragapane, A. H.; Zhao, J.; Han, H. S.; Manoharan, H. C.; Abild-Pedersen, F.; et al. *Nat. Mater.* **2015**, *15*, 48–53.

(24) Tao, L.; Duan, X.; Wang, C.; Duan, X.; Wang, S. *Chem. Commun.* **2015**, *51*, 7470–7473.

(25) Li, G.; Zhang, D.; Qiao, Q.; Yu, Y.; Peterson, D.; Zafar, A.; Kumar, R.; Curtarolo, S.; Hunte, F.; Shannon, S.; et al. *J. Am. Chem. Soc.* **2016**, *138*, 16632–16638.

(26) Wang, H.; Lu, Z.; Xu, S.; Kong, D.; Cha, J. J.; Zheng, G.; Hsu, P.-C.; Yan, K.; Bradshaw, D.; Prinz, F. B.; et al. *Proc. Natl. Acad. Sci.* **2013**, *110*, 19701–19706.

(27) Yin, Y.; Han, J.; Zhang, Y.; Zhang, X.; Xu, P.; Yuan, Q.; Samad, L.; Wang, X.; Wang, Y.; Zhang, Z.; et al. *J. Am. Chem. Soc.* **2016**, *138*, 7965–7972.

(28) Wang, H.; Lu, Z.; Kong, D.; Sun, J.; Hymel, T. M.; Cui, Y. *ACS Nano* **2014**, *8*, 4940–4947.

(29) Tan, C.; Luo, Z.; Chaturvedi, A.; Cai, Y.; Du, Y.; Gong, Y.; Huang, Y.; Lai, Z.; Zhang, X.; Zheng, L.; et al. *Adv. Mater.* **2018**, *30*, 1705509.

(30) Liu, L.; Wu, J.; Wu, L.; Ye, M.; Liu, X.; Wang, Q.; Hou, S.; Lu, P.; Sun, L.; Zheng, J.; et al. *Nat. Mater.* **2018**, *17*, 1108–1114.

(31) Li, Y.; Wang, H.; Xie, L.; Liang, Y.; Hong, G.; Dai, H. *J. Am. Chem. Soc.* **2011**, *133*, 7296–7299.

(32) Yan, Y.; Ge, X.; Liu, Z.; Wang, J.-Y.; Lee, J.-M.; Wang, X. *Nanoscale* **2013**, *5*, 7768–7771.

(33) Li, D. J.; Maiti, U. N.; Lim, J.; Choi, D. S.; Lee, W. J.; Oh, Y.; Lee, G. Y.; Kim, S. O. *Nano Lett.* **2014**, *14*, 1228–1233.

(34) Seo, B.; Jung, G. Y.; Sa, Y. J.; Jeong, H. Y.; Cheon, J. Y.; Lee, J. H.; Kim, H. Y.; Kim, J. C.; Shin, H. S.; Kwak, S. K.; et al. *ACS Nano* **2015**, *9*, 3728–3739.

(35) Vrubel, H.; Hu, X. *ACS Catal.* **2013**, *3*, 2002–2011.